LOW-BANDWIDTH IMAGE RECONSTRUCTION FOR MAGNETIC PARTICLE IMAGING

A THESIS SUBMITTED TO

THE GRADUATE SCHOOL OF ENGINEERING AND SCIENCE

OF BILKENT UNIVERSITY

IN PARTIAL FULFILLMENT OF THE REQUIREMENTS FOR

THE DEGREE OF

MASTER OF SCIENCE

IN

ELECTRICAL AND ELECTRONICS ENGINEERING

By

Damla Sarıca

June 2017

LOW-BANDWIDTH IMAGE RECONSTRUCTION FOR MAGNETIC PARTICLE IMAGING
By Damla Sarıca
June 2017

We certify that we have read this thesis and that in our opinion it is fully adequate, in scope and in quality, as a thesis for the degree of Master of Science.

Emine Ülkü Sarıtaş (Advisor)

Tolga Çukur

İmam Şamil Yetik

Approved for the Graduate School of Engineering and Science:

Ezhan Karaşan
Director of the Graduate School

ABSTRACT

LOW-BANDWIDTH IMAGE RECONSTRUCTION FOR MAGNETIC PARTICLE IMAGING

Damla Sarıca
M.S. in Electrical and Electronics Engineering
Advisor: Emine Ülkü Sarıtaş
June 2017

Magnetic Particle Imaging (MPI) is a high contrast tracer imaging modality with applications such as stem cell tracking, angiography and cancer imaging. In MPI, a time-varying magnetic field called the drive field is applied, and the magnetization response of superparamagnetic iron oxide nanoparticles (SPIOs) is recorded. The signal from these nanoparticles is at both drive field frequency and its higher harmonics. However, due to simultaneous excitation and signal reception, the direct feedthrough contaminates the nanoparticle signal at the fundamental harmonic. The direct feedthrough signal can be eliminated using a high-pass filter, where the effect of this filtering has been shown to be a DC loss in image domain. Reliable x-space image reconstruction can then be achieved via enforcing positivity and continuity of the image. However, low SPIO concentrations and/or hardware constraints can further limit the usable signal bandwidth to only a few harmonics. Under low bandwidth signal acquisitions, the loss of higher harmonics results in blurred images after regular x-space reconstruction. This thesis proposes an iterative x-space reconstruction method that recovers not only the lost fundamental harmonic but also the un-acquired higher harmonics for low-bandwidth acquisitions. Proposed method converges to the ideal (i.e., high bandwidth) MPI image in 3-4 iterations. In extensive simulations that incorporate measurement noise and nanoparticle relaxation effects, the proposed method displays improved image quality with respect to the regular x-space reconstruction scheme, with at least 6 dB improvement in peak signal-to-noise ratio (PSNR) metric. Finally, the proposed method is also demonstrated with imaging experiments on an in-house MPI scanner.

Keywords: Magnetic Particle Imaging, Image Reconstruction, Low-Bandwidth Signal Acquisition.

ÖZET

MANYETİK PARÇACIK GÖRÜNTÜLEME İÇİN DÜŞÜK BANTLI GÖRÜNTÜ GERİÇATIMI

Damla Sarıca
Elektrik ve Elektronik Mühendisliği, Yüksek Lisans
Tez Danışmanı: Emine Ülkü Sarıtaş
Haziran 2017

Manyetik Parçacık Görüntüleme (MPG), kök hücre takibi, anjiyografi ve kanser görüntüleme gibi uygulamalara sahip yüksek kontrastlı bir görüntüleme yöntemidir. MPG'de, eksitasyon alanı adında zamanla değişen bir manyetik alan uygulanır ve süperparamanyetik demir oksit nanoparçacıklarının mıknatıslanma tepkisi kaydedilir. Bu parçacıklardan gelen sinyal hem eksitasyon frekansında hem de bu frekansın yüksek harmoniklerindedir. Eşzamanlı eksitasyon ve sinyal alımı nedeniyle, doğrudan besleme sinyali manyetik nanoparçacık sinyalini ana harmonikte baskılar. Doğrudan besleme sinyali bir yüksek geçiren filtre kullanılarak ortadan kaldırılabilir, ki bu filtrelemenin görüntü uzayında bir DC kaybına neden olduğu gösterilmiştir. X-uzayında güvenilir görüntü geriçatımı, görüntünün pozitifliğini ve sürekliliğini sağlamak yoluyla başarılabilir. Fakat, düşük nanoparçacık konsantrasyonu ve/veya donanım kısıtlamaları, kullanılabilir sinyal bant genişliğini sadece birkaç harmoniğe sınırlayabilir. Normal x-uzayı geriçatımında düşük bantlı sinyal alımı, yüksek harmoniklerin kaybı nedeniyle bulanık görüntülere sebep olmaktadır. Bu tezde, sadece kayıp ana harmoniği değil, aynı zamanda düşük bantlı sinyal alımında kaydedilmemiş yüksek harmonikleri de belirlemeyi sağlayan yinelemeli bir x-uzayı geriçatım yöntemi önerilmektedir. Önerilen yöntem, ideal (yani, yüksek bantlı) MPG görüntüsüne 3-4 yinelemede yakınsar. Gürültü ve nanoparçacık relaksasyon etkilerini içeren kapsamlı simülasyonlarda, önerilen yöntem normal x-uzayı geriçatımına göre gelişmiş görüntü kalitesi vermektedir, ve doruk sinyal gürültü oranında (DSGO) en az 6 dB iyileşme sağlar. Son olarak, önerilen yöntem kendi bünyemizde geliştirdiğimiz MPG tarayıcısında deneysel görüntüler üzerinde de gösterilmiştir.

Anahtar sözcükler: Manyetik Parçacık Görüntüleme, Görüntü Geriçatımı, Düşük Bantlı Sinyal Alımı.

Acknowledgement

I owe my deepest gratitudes to my advisor, Asst. Prof. Dr. Emine Ülkü Sarıtaş, for giving me an opportunity of M.Sc. degree in Bilkent University, supporting me throughout my graduate studies and showing me guidance whenever I needed throughout this thesis.

I would like to thank Asst. Prof. Dr. Tolga Çukur and Assoc. Prof. Dr. İmam Şamil Yetik for being a member in my thesis committee.

I would like to thank the following funding sources for supporting the work in this thesis: the Scientific and Technological Research Council of Turkey (TUBITAK 114E167), the European Commission FP7 Marie Curie Career Integration Grant (PCIG13-GA-2013-618834), TUBA-GEBIP 2015 program of the Turkish Academy of Sciences, and the BAGEP Award of the Science Academy.

I also want to thank all of my lab members: Ecem Bozkurt, Çağla Deniz Bahadır, Ömer Burak Demirel, Sevgi Gökçe Kafalı, Toygan Kılıç, Yavuz Muslu, Ali Alper Özaslan, Kalaivani Thangavel, Mustafa Ütkür and Serhat İlbey for their valuable friendship, support and contributions to me and my work.

I would like to thank my closest and dearest friends Merve Uzun and Emir Artık for their support and valuable friendship during my university years.

I also want to thank Caner Asbaş, Tuba Ceren Deveci, Akbar Alipour, Mohammad Tofighi, Caner Odabaş, Oğuzhan Oğuz, Tunç Arslan and Merve Begüm Terzi for their friendship and support.

There are many precious people in Bilkent, who are like a family to me. I would like to thank Mürüvet Parlakay, Ergün Hırlakoğlu, Onur Bostancı, Ufuk Tufan, Aydan Ercingöz and Ebru Ateş.

I dedicate this thesis to my uncle and aunt-in-law, Cevat and Tülay Kömürcü, my parents, Sevim and Aydın, and my beloved sister, Yudum. No words can express my gratitude to them. I believe that I can always motivate myself to be successful with their endless love and support.

Contents

List of Figures

List of Tables

Chapter 1

Introduction

Magnetic Particle Imaging (MPI) is a new, noninvasive, tracer imaging modality that was first presented in 2005 [1, 2]. This imaging modality utilizes non-linear magnetization behavior of superparamagnetic iron oxide nanoparticles (SPIOs) under static and dynamic magnetic fields. SPIOs are safe-contrast agents as opposed to gadolinium- or iodine-based contrast agents, especially for patients who suffer from chronic kidney disease (CKD) [3]. MPI enables imaging with high resolution and high sensitivity for animal and human imaging [4]. MPI is developing rapidly since there are many advances in applications, nanoparticles, hardware, and image processing [5, 6, 7, 8, 9, 10]. In x-space MPI, on the other hand, the image is reconstructed directly in spatial domain via gridding the velocity compensated signal to the scanned position [11].

In MPI, a localized region with zero static magnetic field, called the field free point (FFP), is created using the strong gradient of a magnetic field called the selection field. The FFP is moved over an imaging field-of-view (FOV) using drive fields (i.e., excitation fields) in all three directions. When the FFP passes over a SPIO nanoparticle in the FOV, the change in the SPIO magnetization induces signal in a receive coil. This signal includes energy at the drive field frequency and its higher harmonics. The MPI image can then be reconstructed for a given FOV using the received signal at all harmonics. The advances in image reconstruction in MPI provide to obtain more realistic and reliable reconstructed images. In MPI, there are two possible image reconstruction techniques and they are based on system function and x-space approaches. In system function approach [12, 13], high calibration scan time is required and image is reconstructed using frequency domain. In x-space MPI, the image is reconstructed directly in spatial domain [11].

The field-of-view (FOV) size is proportional to the drive field amplitude and inversely proportional to the gradient of the selection field. The human safety limits determine the maximum field strength for the drive field and this restricts the size of the FOV to a few centimeters [3, 14, 15, 16]. For human imaging applications, much larger FOV sizes are required. Therefore, the concept of focus field was introduced in MPI, where applying the drive field together with a much slower focus field enlarges the FOV covered by the FFP [2, 17]. In this scanning scheme, each small imaging region covered due to the drive field only is called a partial-FOV (pFOV), or image patch.

The SPIOs respond to the applied magnetic field almost instantaneously, therefore; simultaneous excitation and signal reception is required and this causes a direct feedthrough signal problem at the drive field frequency [18]. In the received signal spectrum, the direct feedtrough signal occuring at the drive field frequency is orders of magnitude higher than the SPIO signal. Luckily, SPIO signals are obtained both at the drive field frequency and its higher harmonics. Therefore, using a gradiometer-type receive coil together with analog/digital high-pass filters, the direct feedthrough signal can be removed successfully. However, together with the direct feedthrough signal, the SPIO signal at the fundamental harmonic is also removed. In spatial domain, the loss of the first harmonic corresponds to different amounts of DC (constant) loss for each pFOV. Since it is known that the reconstructed SPIO distribution cannot be negative and it should be a continuous function of space, it is possible to recover the lost DC information for each pFOV and reconstruct the MPI image [11, 12, 18]. This method is also known as "DC loss recovery" in regular x-space image reconstruction.

In theory, the ideal MPI image can be reconstructed using all harmonics

[11, 12, 18]. However, in practice, hardware limitations (e.g., the self-resonance of the receive coil) or low concentration levels of the SPIOs can make only a few harmonics usable. Typically, the signal from the nanoparticles decreases rapidly at higher harmonics. Hence, in the case of low dose administrations or for systems with less than desirable sensitivities, the nanoparticle signal may reach the noise floor after only a few harmonics. Nanoparticle type (i.e., particle size and structure), the environment of the nanoparticle (i.e., liquid or solid samples) [19] or the core size distribution of the nanoparticles [20] are the main factors that determine how rapidly the signal harmonics at the higher harmonics fall. Under low bandwidth acquisitions, regular x-space image reconstruction results in blurred images due to the loss of higher harmonic components.

In this thesis, an iterative x-space reconstruction algorithm that recovers not only the lost fundamental harmonic but also the un-acquired higher harmonics is proposed. First of all, the relation between the ideal MPI image and the lost DC components is derived and it is shown that this relation can be expressed as the convolution of the ideal image with a known kernel. Therefore, as an alternative way, ideal MPI image in the case of high bandwidth acquisitions can be reconstructed via deconvolving the recovered DC components by the known convolution kernel. Secondly, a projection onto convex sets (POCS) type iterative approach that sequentially enforces data consistency and DC loss consistency is presented for low bandwidth data acquisitions. Through both simulations and imaging experiments, the improvements achieved via this image reconstruction technique is demonstrated. It is shown that the proposed method successfully recovers the un-acquired higher harmonics for low bandwidth acquisitions and displays at least 6 dB improved peak SNR when compared to the regular x-space reconstruction.

Chapter 2

Magnetic Particle Imaging: Principles and Background

2.1 Magnetic Nanoparticle Magnetization

Magnetic Particle Imaging (MPI) relies on the nonlinear magnetization behaviour of superparamagnetic iron oxide (SPIO) nanoparticles, as explained by the Langevin theory. According to Langevin theory, nanoparticles are assumed to be in thermal equilibrium and their behavior is described by their magnetic moment m. Each superparamagnetic nanoparticle experiences Brownian motion; therefore, there is randomness in the distribution of the magnetic moments of each nanoparticle. In a larger scale, the net magnetic moment for an ensemble of nanoparticles becomes zero. Magnetization, M, is the density of the sum of all magnetic moments and can be represented as [21]:

$$M := \sum_{i=0}^{N-1} m_i \frac{1}{\Delta V} \tag{2.1}$$

Here, N is the number of nanoparticles located at a small volume, ΔV. If there is an external magnetic field, magnetic nanoparticles start to align with the applied magnetic field until a certain threshold value. Above this threshold value, superparamagnetic nanoparticles go into a saturation region. In this region even if the applied magnetic field changes, the magnetization does not change [21]. The overall SPIO magnetization behavior can be described by the Langevin function, $\mathcal{L}$, as shown in Figure 2.1.

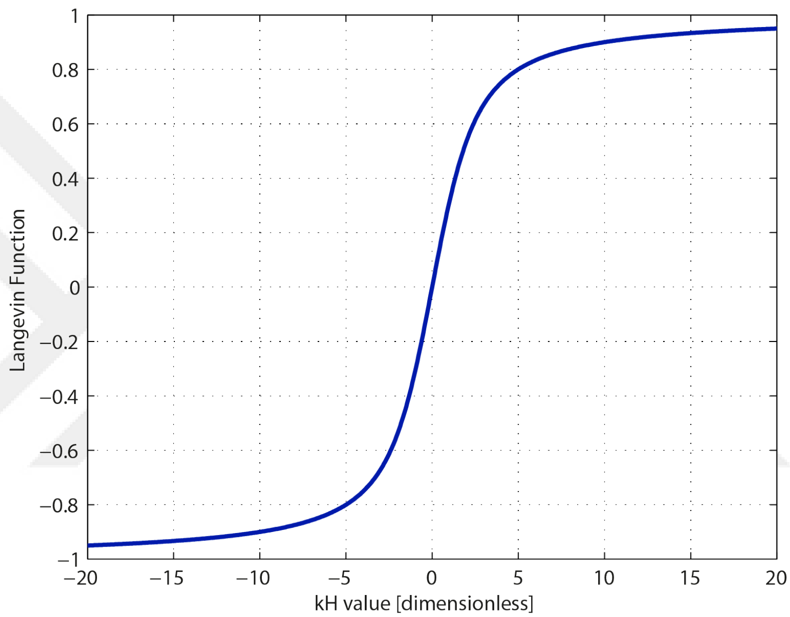

Figure 2.1: Relation between applied magnetic field, H, and magnetization, M.

Nanoparticle magnetization, M, can be expressed in terms of applied magnetic field, H, as below:

$$M(H) = c(x)\, m\, \mathcal{L}(kH) \tag{2.2}$$

Here, $c(x)$ is the nanoparticle concentration, k is a property of the magnetic nanoparticle and Langevin function, $\mathcal{L}$, can be represented as:

$$\mathcal{L}(\zeta) = \begin{cases} \coth(\zeta) - \frac{1}{\zeta} & \text{if } \zeta \neq 0 \\ 0 & \text{if } \zeta = 0 \end{cases} \tag{2.3}$$

and

$$k := \frac{\mu_0 m}{k_B T} \tag{2.4}$$

Here, μ_0 is the permeability of free space, k_B is the Boltzmann constant and T is the temperature of the superparamagnetic nanoparticles.

The derivative of the Langevin function, $\dot{\mathcal{L}}$, is the point spread function (PSF) of one-dimensional MPI system.

$$\dot{\mathcal{L}}(\zeta) = \begin{cases} \frac{1}{\zeta^2} - \frac{1}{\sinh^2(\zeta)} & \text{if } \zeta \neq 0 \\ \frac{1}{3} & \text{if } \zeta = 0 \end{cases} \tag{2.5}$$

The Full-Width-at-Half-Maximum (FWHM) is the resolution for this imaging modality and it is approximately 4.16 [21].

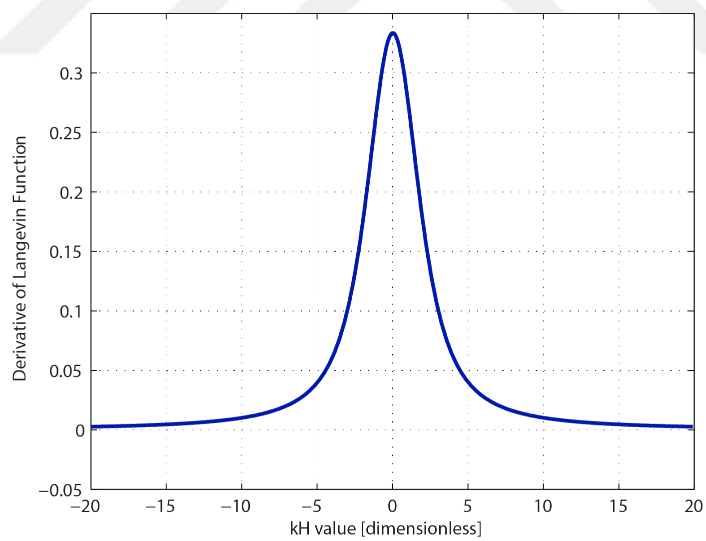

Figure 2.2: The derivative of the Langevin function is the PSF of the Magnetic Particle Imaging.

FWHM can be found using the formula given below as [12]:

$$FWHM \approx \frac{4k_B T}{\mu_0 G m}[m] \ \approx \frac{24 k_B T}{\mu_0 \pi M_{sat}} G^{-1} d^{-3} [m] \tag{2.6}$$

Here, G is the gradient strength, $M_{sat} \approx 0.6\ T/\mu_0$ and d is the diameter of the magnetic nanoparticle. Accordingly, the resolution can be improved by increasing the gradient strength of the selection field or nanoparticle diameter. Although it seems like increasing particle diameter will indefinitely improve the imaging resolution, in reality the relaxation behavior of the magnetic nanoparticles limits that trend. This behavior and its effects on the nanoparticle magnetization and MPI signal are explained in the next section.

2.2 Magnetic Nanoparticle Relaxation Effects

As it is stated in the previous section, Langevin theory explains the magnetic behavior of the magnetic nanoparticle assuming thermal equilibrium. Thermal equilibrium condition is satisfied when the applied magnetic field and the magnetization are in the same direction. That is, under static magnetic field, thermal equilibrium is valid. However, if there is an applied time-varying magnetic field, the magnetization of the magnetic nanoparticle can not be aligned with the time-varying magnetic field immediately [22, 23, 24, 25]. There is a delay in the response of the magnetic nanoparticle magnetization. The nanoparticle magnetization under thermal equilibrium where nanoparticle relaxation effect is assumed as negligible is defined using adiabatic theory [23].

$$M_{adiab}(t) = m\,\rho(x)\,\mathcal{L}(kH(t)) \tag{2.7}$$

Here, $H(t)$ is the applied magnetic field and $1/k$ determines how easily the magnetic nanoparticle can go into saturation region. If there is a time-varying magnetic field, then the nanoparticle magnetization becomes non-adiabatic and can be described as:

$$M(t) = M_{adiab}(t) * \frac{1}{\tau}\, exp\left(\frac{-t}{\tau}\right) u(t) \tag{2.8}$$

Above equation can be simplified as the temporal convolution of adiabatic magnetization and a convolution kernel as:

$$M(t) = M_{adiab}(t) * r(t) \tag{2.9}$$

The relaxation effect on the magnetic nanoparticle magnetization is dependent on the applied magnetic field frequency. If the frequency is slow such that the magnetic nanoparticle can respond to the change of the time-varying magnetic field immediately, then the adiabatic theory and Langevin function are sufficient to describe the nanoparticle behavior. However, if the frequency of the magnetic field is in the range of $\frac{1}{\tau}$, then magnetic nanoparticle can not be aligned with the applied magnetic field and the non-adiabatic magnetization becomes valid. If the frequency of magnetic field is further increased, then it is impossible for the nanoparticle to keep up with the applied magnetic field and respond to it immediately. In this case, the amplitude of the magnetic nanoparticle signal decreases and MPI method does not work [21].

There are two relaxation types that affect the magnetic nanoparticle in the existence of the time-varying magnetic field. The first one is the Brownian relaxation, which causes a physical rotation and the second one is the Néel relaxation, which is the rotation of the magnetic moments in the magnetic nanoparticle. If the medium is viscous, both relaxation processes take place simultaneously, and the dominant one determines the effective relaxation time. The behaviors of both relaxation types can be seen from Figure 2.3.

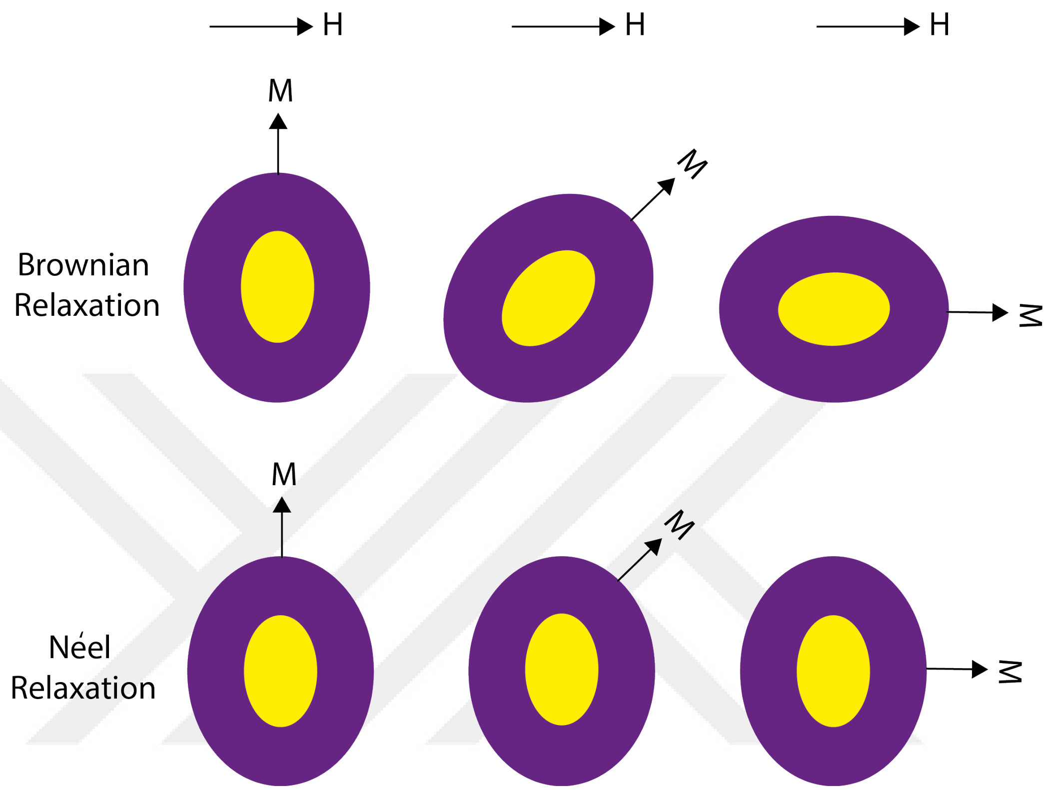

Figure 2.3: Comparison of Brownian and Néel Relaxation. Brownian relaxation occurs with a physical rotation of the magnetic nanoparticle and Néel relaxation occurs with an internal change of the magnetic nanoparticle moment.

Relaxation time constant for the Brownian motion can be found using the below formula:

$$\tau_B = \frac{3\eta V_H}{k_B T} \tag{2.10}$$

Relaxation time constant for the Néel motion can be found using the below formula:

$$\tau_N = \tau_0 \; exp\left(\frac{K_A V}{k_B T}\right) \tag{2.11}$$

Here, η is the viscosity of the environment, V_H is the hydrodynamical volume, k_B is the Boltzmann constant, T is the particle temperature, K_A is the anisotropy constant and V is the particle core volume. While Brownian relaxation time constant is dependent on the hydrodynamical volume, N$\acute{e}$el ralaxation time constant is dependent on the nanoparticle core volume. In the lower frequency range, Brownian motion and Brownian relaxation time constant are dominant and in the higher frequency range N$\acute{e}$el motion and N$\acute{e}$el relaxation time constant are dominant [21]. Overall, the two relaxation processes can be considered as parallel processes, which can be expressed as follows:

$$\tau = \left(\frac{\tau_B \ \tau_N}{\tau_B \ + \tau_N} \right) \tag{2.12}$$

2.3 1-D Signal and Image Equations

In MPI, the change in magnetic nanoparticle magnetization gives opportunity to have information about nanoparticle concentration. To induce a change in the magnetization of the nanoparticles, a time-varying magnetic field is applied via drive coils. There are also receive coils to measure magnetization change since magnetic nanoparticles induce voltage into the receive coils. If the relaxation effects are not considered, the signal can be represented as follows [11, 23]:

$$s_{adiab}(t) = -\frac{d}{dt} \int_{object} B_1 \ M_{adiab}(r,t) \ dr \tag{2.13}$$

Here, B_1 is the receive coil sensitivity.

$$s_{adiab}(t) = \dot{x}_s(t) \ \Upsilon \ \left\{ \rho(x) * \dot{\mathcal{L}}(kGx) \right\} \Big|_{x=x_s(t)} \tag{2.14}$$

Here, $x_s(t)$ is the position of the FFP as a function of time, $\Upsilon = B_1 kmG$ and $\dot{x}_s(t)$ is FFP velocity. Therefore, adiabatic particle density can be written as the velocity compensated signal, assigned to the instantaneous position of the FFP, i.e.,

$$\hat{\rho}_{adiab}(x_s(t)) = \frac{s_{adiab}(t)}{\Upsilon \dot{x_s}(t)} \tag{2.15}$$

Therefore, 1-D particle concentration can be expressed in terms of Langevin function as:

$$\hat{\rho}_{adiab}(x_s(t)) = \rho(x) \; * \; \dot{\mathcal{L}}(kGx)|_{x=x_s(t)} \tag{2.16}$$

In the non-adiabatic theory, the signal is the temporal convolution of the adiabatic signal with relaxation convolution kernel, $r(t)$ [23].

$$s(t) = s_{adiab}(t) * r(t) \tag{2.17}$$

Here, $r(t) = \frac{1}{\tau} exp\left(\frac{-t}{\tau}\right) u(t)$. Due to the delay in the signal response, simple division by velocity does not yield accurate results as in the adiabatic theory. One method to alleviate the problems caused by the delay between the signal and velocity is to perform a shift of approximately $\frac{\tau}{2}$, i.e., :

$$\hat{\rho}(x_s(t)) = \frac{s(t)}{\Upsilon \dot{x_s}(t - \frac{\tau}{2})} \tag{2.18}$$

In the simulations and experiments, it was shown that below approximation can be used for the above equation:

$$\hat{\rho}(x_s(t)) \approx \left(\rho(x) \; * \; \dot{\mathcal{L}}(kGx)|_{x=x_s(t)}\right) \; * r(t) \tag{2.19}$$

2.4 Multidimensional Signal and Image Equations

In multidimensional signal acquisition, the signal equation becomes more complex when compared to the 1-D signal acquisition and the acquired signal can be written as [26]:

$$s(t) = B_1(x) m\rho(x) *** k \; ||\dot{x}_s|| h(x) \hat{\dot{x}}_s \big|_{x=x_s(t)} \tag{2.20}$$

Here, h(x) is the PSF of the multidimensional x-space MPI (see Figure 2.4) and equivalent to below expression:

$$h(x) = \dot{\mathcal{L}}(k \; ||Gx||) \frac{Gx}{||Gx||} \left(\frac{Gx}{||Gx||} \right)^T G + \frac{\mathcal{L}(k \; ||Gx||)}{k|||Gx||} \Big(I - \frac{Gx}{||Gx||} \left(\frac{Gx}{||Gx||} \right)^T \Big) G \tag{2.21}$$

Here, G is the vector of selection field gradient strengths in all 3 directions, and x is the position vector. Therefore, multidimensional x-space MPI image can be formulated as:

$$\hat{\rho}(x_s(t)) = \rho(x) *** \hat{\dot{x}}_s. \;\; h(x) \; \hat{\dot{x}}_s \big|_{x=x_s(t)} \tag{2.22}$$

Here, as it can be seen from the multidimensional imaging equation, the PSF is dependent on both $\mathcal{L}$ and $\dot{\mathcal{L}}$.

2.5 Direct Feedthrough Problem in MPI

In MPI, a time-varying magnetic field called drive field (or excitation field) is applied to the magnetic nanoparticles and the magnetization response of the SPIOs is recorded. When the received spectrum is analyzed, it can be seen that the magnetic nanoparticle signal is both at the drive field frequency and its higher

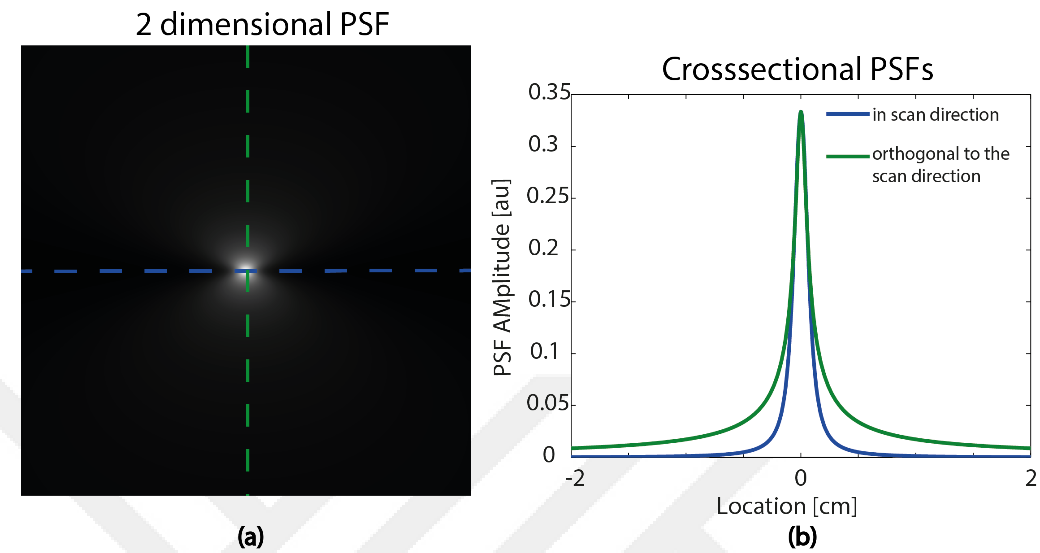

Figure 2.4: Multidimensional PSF. a) 2 Dimensional PSF and b) cross-sectional profiles of the PSF along the scan direction and orthogonal to the scan direction. In the scan direction, PSF is narrower.

harmonics. The excitation and the signal reception should be at the same time. However, due to the simultaneous excitation and signal reception, a significant amount of direct feedthrough interference is induced in the receive coil by the drive field at the fundamental frequency. The direct feedthrough contamination is orders of magnitude larger than the magnetic nanoparticle signal. One solution to eliminate the direct feedthrough signal is to use a high-pass filter. Although the high-pass filter removes the direct feedthrough signal, it also causes the loss of magnetic nanoparticle signal at the fundamental frequency, as shown in Figure 2.5. It has been shown that the loss of the fundamental frequency signal corresponds to a DC loss in image domain [18].

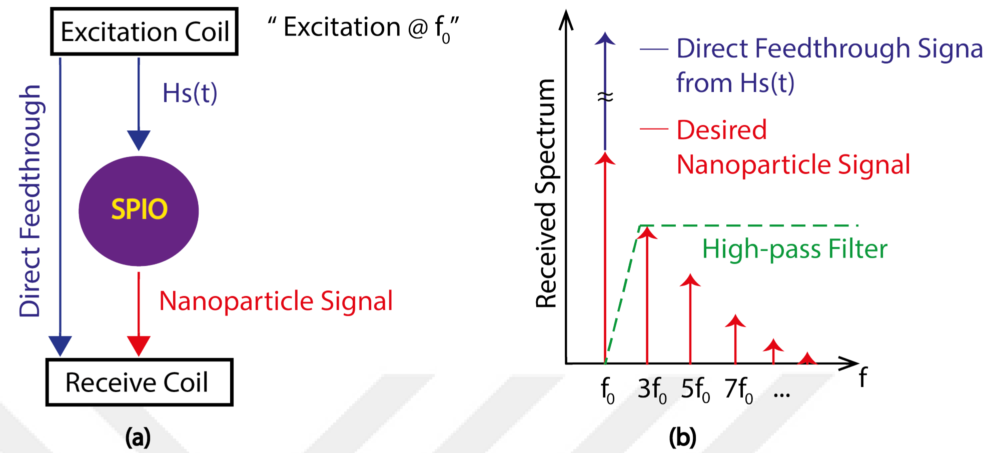

Figure 2.5: Direct feedthrough problem in MPI. a) The simultaneous excitation and signal reception results in direct feedthrough signal at the fundamental frequency (block diagram). b) The direct feedthrough signal supresses the desired magnetic nanoparticle signal. The solution is to use a high-pass filter to remove the direct feedthrough contamination.

Luckily, it is possible to recover this loss in image domain. The aim in MPI is to image the concentration of the magnetic nanoparticles, which cannot be negative valued. Therefore, it is possible to remove the image artifact due to the high-pass filtering of the fundamental frequency signal by enforcing nonnegativity in the image domain, as shown in Figure 2.6 [18].

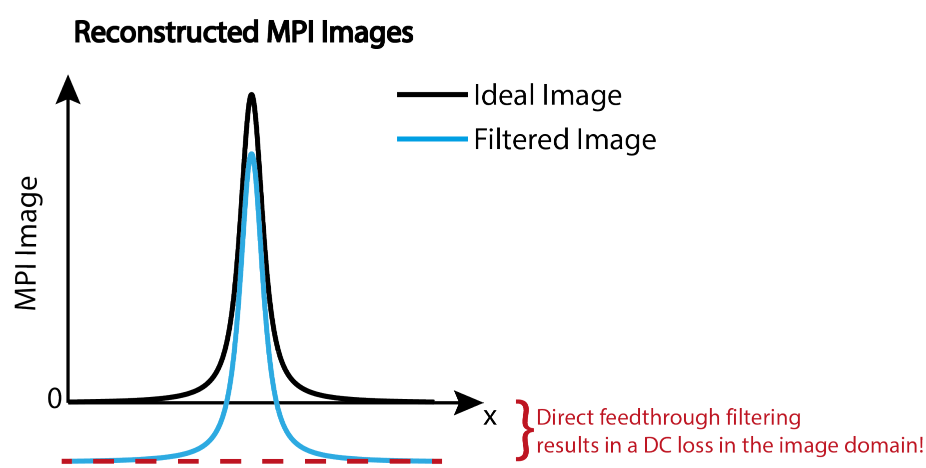

Figure 2.6: The loss of the fundamental frequency signal corresponds to a DC loss in image domain.

2.6 Scanning and Image Reconstruction in MPI

The human safety limits of time-varying magnetic fields restrict the maximum field strength for the drive field, limiting the size of the FOV to a few centimeters [14, 15, 16]. Since human imaging applications require much larger FOVs, the concept of focus field was introduced in MPI [2, 17]. Applying the drive field together with a much slower focus field effectively enlarges the imaging region covered by the FFP. In this scanning scheme, each small imaging region covered due to the drive field only is called as the partial FOV (pFOV), or the image patch.

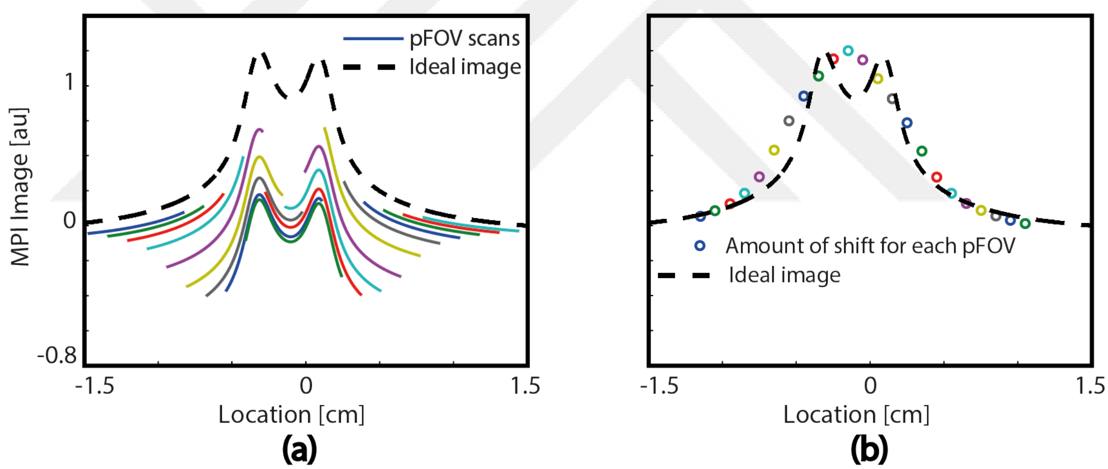

Figure 2.7: Scanning and image reconstruction in MPI. a) The loss of the fundamental frequency signal corresponds to different and unknown amounts of DC loss for each pFOV b) Due to the overlapping sections of neighboring pFOVs, it is possible to calculate the needed amount of shift for each pFOV.

After direct feedthrough filtering, each pFOV experiences a different amount of DC loss. Luckily, neighboring pFOVs have overlapping sections. Hence, one can calculate the amount of shift needed for each pFOV, as shown in Figure 2.7. Enforcing both the nonnegativity and continuity in image domain, it is possible to recover the ideal MPI image, as shown in Figure 2.8 [18].

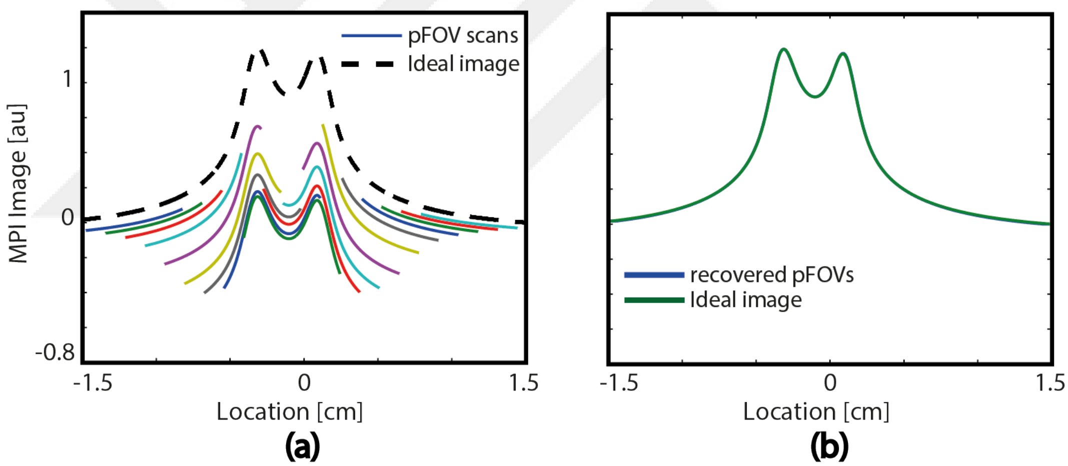

Figure 2.8: DC Recovery Algorithm. a) The loss of the fundamental frequency signal corresponds to different and unknown amounts of DC loss for each pFOV b) Using DC recovery algorithm, it is possible to recover ideal MPI image.

Chapter 3

Theory

3.1 DC Shift Theory

The ideal MPI image in x-space MPI, $\hat{\rho}(x)$, can be expressed as the convolution of the nanoparticle distribution, $\rho(x)$, with a Langevin-based MPI point spread function (PSF), h(x), as [11]:

$$\hat{\rho}(x_s(t)) = \rho(x) \ * \dot{\mathcal{L}}(kGx)\Big|_{x=x_s(t)} \tag{3.1}$$

$$= \rho(x) \ * h(x)\Big|_{x=x_s(t)} \tag{3.2}$$

Here, $\dot{\mathcal{L}}$ is the derivative of the Langevin function, k is a property of a nanoparticle, G is the selection field gradient and $x_s(t)$ is the field-free-point (FFP) position. This simple image equation is valid for one-dimensional case. For multi-dimensional MPI, the Langevin-based MPI PSF depends both $\dot{\mathcal{L}}$ and $\mathcal{L}$, as well as the drive field direction [26].

The ideal MPI image can also be calculated using the harmonic decomposition of the ideal magnetic nanoparticle signals as [18]:

$$\hat{\rho}(x) = \alpha \sum_{k=1}^{\infty} S_k \; U_{k-1}\left(\frac{2x}{W}\right) \tag{3.3}$$

Here, S_k is the k^{th} harmonic term, which can be described as:

$$S_k = \beta \int_{-\frac{W}{2}}^{\frac{W}{2}} \hat{\rho}(x) \; U_{k-1}\left(\frac{2x}{W}\right) \; \sqrt{1 - \left(\frac{2x}{W}\right)^2} \; dx \tag{3.4}$$

where α is $(-kB_1mG\pi f_0W)^{-1}$, β is $-4kB_1mGf_0$, $U_{k-1}(.)$ is the simple Chebyshev polynomial of the second kind, W is the total extent of the pFOV and $\sqrt{1-(2x/W)^2}$ is the space-variant velocity term.

The filtering of the drive field frequency component causes the loss of the first harmonic, S_1, term. This loss can be mathematically expressed as:

$$S_1 = \beta \int_{-\frac{W}{2}}^{\frac{W}{2}} \hat{\rho}(x) \; U_0\left(\frac{2x}{W}\right) \; \sqrt{1 - \left(\frac{2x}{W}\right)^2} \; dx \tag{3.5}$$

Here, the first Chebyshev polynomial of the second kind, $U_0\left(\frac{2x}{W}\right)$, is equal to 1. Therefore, the first harmonic term can be simplified as:

$$S_1 = \beta \int_{-\frac{W}{2}}^{\frac{W}{2}} \hat{\rho}(x) \; \sqrt{1 - \left(\frac{2x}{W}\right)^2} \; dx \tag{3.6}$$

The image information that is lost due to the loss of the fundamental frequency signal can then be calculated as:

$$\hat{\rho}_{DC}(x) = \alpha S_1 = \alpha\beta \int_{-\frac{W}{2}}^{\frac{W}{2}} \hat{\rho}(x) \; \sqrt{1 - \left(\frac{2x}{W}\right)^2} \; dx \tag{3.7}$$

Since each pFOV experiences different amounts of DC loss, the equation above can be expanded for each pFOV mathematically as follows:

$$S_{1,j} = \beta \int_{-\frac{W}{2}}^{\frac{W}{2}} \hat{\rho}(x_{0j} + x) \sqrt{1 - \left(\frac{2x}{W}\right)^2} \, dx \tag{3.8}$$

Here, $S_{1,j}$ is the amount of DC loss experienced by the j^{th} pFOV and x_{0j} is the center of the j^{th} pFOV. Using the symmetry of the second term in this formulation, the amount of DC loss for each pFOV can be written in the form of a convolution evaluated at the center of each pFOV as:

$$S_{1,j} = \beta \ \hat{\rho}(x) \ * \ h_{DC}(x) \ \Big|_{x=x_{0j}} \tag{3.9}$$

Therefore, the lost first harmonic image information can be calculated using the below formula [27]:

$$\hat{\rho}_{DC}(x_{0j}) = \frac{4}{\pi W} \ \hat{\rho}(x) \ * \ h_{DC}(x) \ \Big|_{x=x_{0j}} \tag{3.10}$$

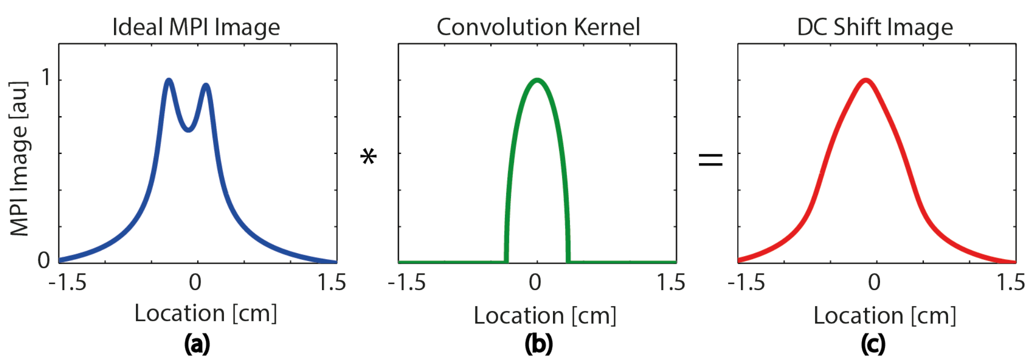

Figure 3.1: Convolution of a) ideal MPI image with a known b) convolution kernel results in c) DC shift image.

In the above formulation, $h_{DC}(x) = \sqrt{1 - (2x/W)^2}$ is the convolution kernel and can be calculated for given scan parameters (see Figure 3.1b). This formulation shows that the DC shift values can be assigned to the center of each pFOV. Using an appropriate interpolation technique, it is possible to obtain a "DC shift image", $\hat{\rho}_{DC}(x)$, for all positions. Here, as the convolution kernel gets narrower (i.e., as the pFOV size W gets smaller), the DC shift image converges to the ideal MPI image. Therefore, one can obtain the ideal MPI image by deconvolving the DC shift image with the known convolution kernel.

3.2 Low-Bandwidth Iterative Reconstruction in MPI

In MPI, hardware limitations (e.g., receive coil self resonance) or low SPIO concentrations may make only a few magnetic nanoparticle harmonics usable. In addition to these, nanoparticle type, structure, core size distribution or the environment can have an important effect on the harmonic intensities [19, 20]. Due to these reasons, low-bandwidth data acquisition may be mandatory. In this section, an iterative image reconstruction technique that can obtain the ideal MPI image is proposed for low-bandwidth acquisitions (e.g., 2^{nd} and 3^{rd} harmonics only).

Under low-bandwidth data acquisition, it is difficult to obtain the ideal MPI image. When regular x-space MPI image reconstruction technique is applied, due to the loss of higher harmonics, the reconstructed image experiences a resolution loss (see Figure 3.2). However, DC shift image, $\hat{\rho}_{DC}(x)$, can be still calculated successfully. Hence, by deconvolving the DC shift image with the known convolution kernel, $h_{DC}(x)$, the deconvolved DC shift image, $\tilde{\rho}(x)$, can be obtained. The deconvolved DC shift image fortunately includes all harmonics information even under low-bandwidth, as shown in Figure 3.3. One can see from Figure 3.3c that despite a considerable improvement over the regular MPI image, there are visible artifacts in the deconvolved DC shift image in the case of 2^{nd} harmonic only. Hence, the minimum bandwidth for the proposed method should include at least the 2^{nd} & 3^{rd} harmonics.

Based on the robustness of the DC shift image against low-bandwidth data acquisitions, this thesis proposes a projection onto convex sets (POCS) method to iteratively enforce data consistency and DC shift consistency. This method yields an image that converges to the ideal MPI image in only a few iterations, as outlined in Figure 3.4.

In the iterative reconstruction process, the image reconstruction starts with low-bandwidth data acquisition. Using the acquired data, it is possible to reconstruct both the DC shift image, $\hat{\rho}_{DC}(x)$, and the regular x-space MPI image,

$\hat{\rho}(x)$. As it can be seen from Figure 3.2, regular x-space image is blurred under low bandwidth due to the loss of higher harmonics. On the other hand, it is possible to obtain the deconvolved DC shift image, $\tilde{\rho}_{j,1}(x)$, which includes all harmonics by deconvolving DC shift image with a known convolution kernel. The low-bandwidth information that belongs to the acquired data is more reliable and is reinforced during the iterative reconstruction. The higher harmonics information can be extracted from the deconvolved DC shift image and combined with the acquired low bandwith image information to reconstruct all harmonics image. At this point, the lost fundamental harmonic information is also calculated from the deconvolved DC shift image and subtracted from the all harmonics image in order to apply regular x-space reconstruction technique.

$$\tilde{S}_{k,j,n} = \beta \int_{-\frac{W}{2}}^{\frac{W}{2}} \tilde{\rho}_n(x_{0j} + x)\ U_{k-1}\left(\frac{2x}{W}\right) \sqrt{1 - \left(\frac{2x}{W}\right)^2}\ dx \tag{3.11}$$

$$\tilde{\rho}_{j,n}(x) = \alpha \sum_{k=1}^{\infty} \tilde{S}_{k,j,n}\ U_{k-1}\left(\frac{2x}{W}\right) \tag{3.12}$$

In the above equations, k, j and n represent the k^{th} harmonic term, j^{th} pFOV and the n^{th} iteration. Therefore, for the next iteration, the reconstructed image can be calculated using the below formula:

$$\hat{\rho}_{j,n+1}(x) = \hat{\rho}_{j,1}(x) + \left\{ \tilde{\rho}_{j,n}(x) - \alpha \sum_{k=1}^{M} \tilde{S}_{k,j,n}\ U_{k-1}\left(\frac{2x}{W}\right) \right\} \tag{3.13}$$

Here, M represents the highest harmonic that can be acquired during low-bandwidth acquisition. Iterative reconstruction is stopped when the reconstructed image, $\hat{\rho}_{j,n+1}(x)$, is expected to converge to the ideal x-space MPI image (i.e., all harmonics).

To determine the number of iterations required to achieve convergence, image reconstruction simulations were done until the 10^{th} iteration. Visually, the convergence is very rapid, and the image improves dramatically in just one iteration. For a quantitative evaluation, peak-signal-to-noise ratio (PSNR) image quality metric can be used to determine the number of iterations required to achieve convergence. The PSNR metric used in this method can be written as:

$$PSNR_{dB} = 10log_{10}\frac{max(I_{ideal}^2)}{MSE} \tag{3.14}$$

Here, I_{ideal} is the ideal MPI image when all harmonics are included, MSE is the mean-squared error between the ideal MPI image and the reconstructed MPI image. As it can be seen from Figure 3.6, for the case of low-bandwidth regular x-space image, the PSNR value is around 30 dB. In the first few iterations of the algorithm, there is a rapid increase in the PSNR results. At the 4^{th} iteration, PSNR converges nearly to 53 dB and does not change with the increasing number of iterations. Therefore, the output image at the 4^{th} iteration can be considered as the output image for the proposed method. The improvement on the reconstructed 2D images can be seen from Figure 3.7.

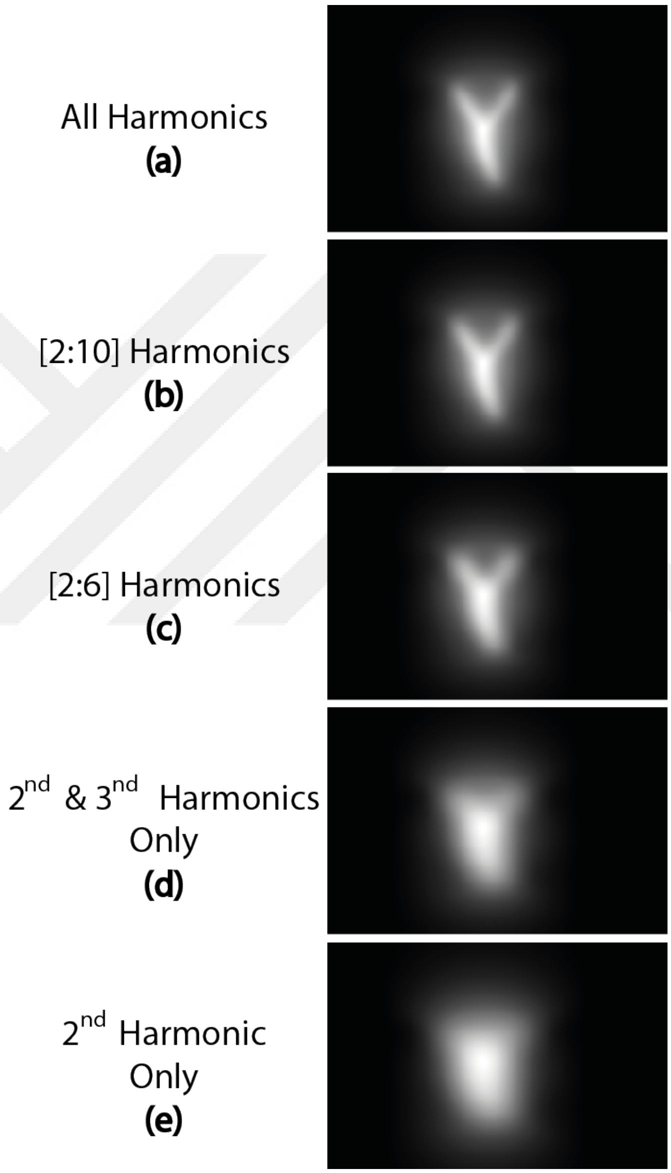

Figure 3.2: Regular x-space reconstruction under low bandwidth results in blurred images. The a) ideal image that includes all harmonics is less blurred. b) Regular x-space MPI image when up to 10^{th} harmonics are included, c) is regular x-space MPI image when up to 6^{th} harmonics are included. d) and e) show the low bandwidth regular x-space MPI images when 2^{nd} & 3^{rd} harmonics and 2^{nd} harmonic only cases are considered, respectively.

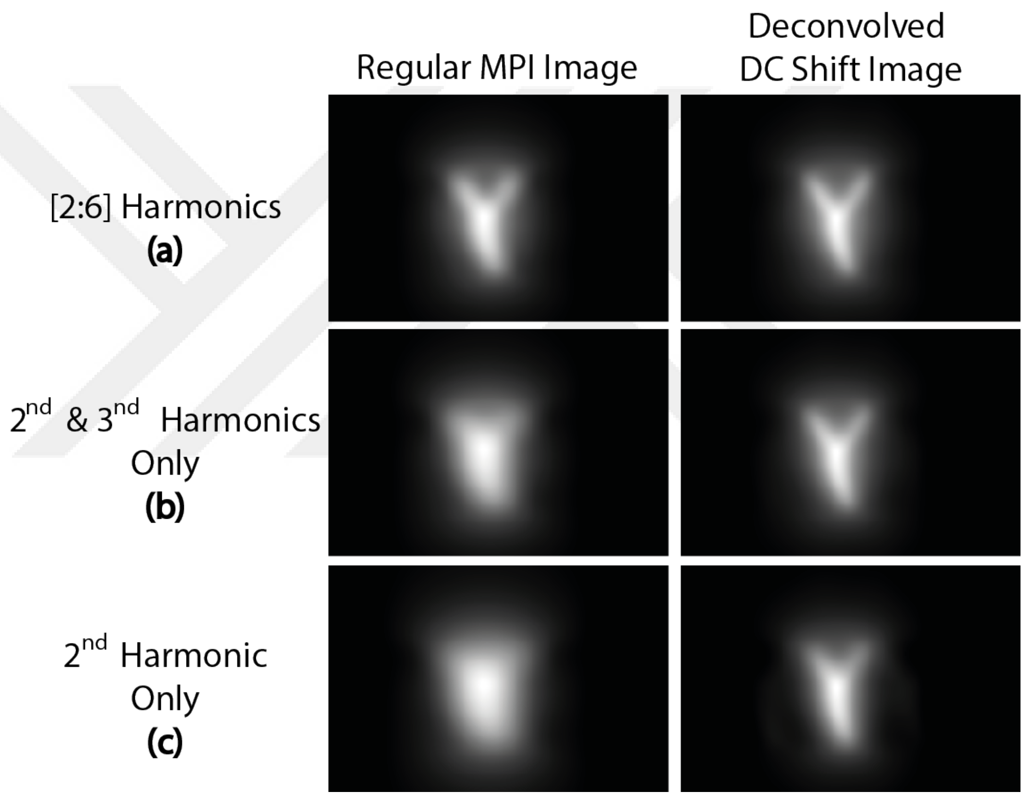

Figure 3.3: Regular x-space reconstruction and deconvolved DC shift images under different bandwidths. Even under low bandwidth, it is possible to reconstruct the deconvolved DC shift image. However, if only 2^{nd} harmonic is acquired, then the deconvolved DC shift image has visible artifacts. Due to this reason, at least 2^{nd} and 3^{rd} harmonics should be acquired. If 2^{nd} and 3^{rd} harmonics are acquired, then the resulting deconvolved DC shift image is very similar to the regular x-space MPI image when all harmonics are included.

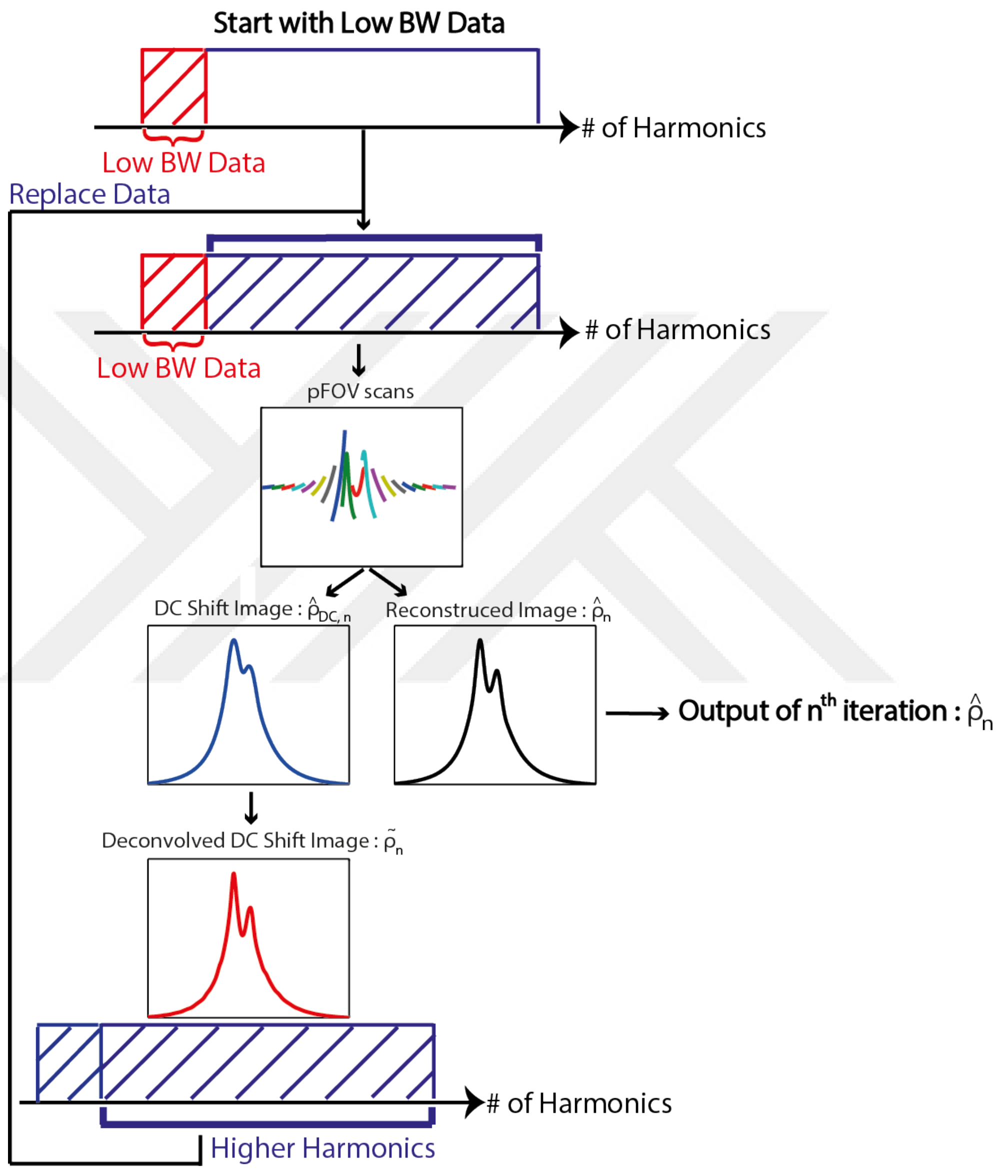

Figure 3.4: The reconstruction starts with a low-bandwidth acquisition and both DC shift and deconvolved DC shift images are calculated, as well as regular x-space MPI image. While regular x-space MPI image includes only low-bandwidth information, due to its nature deconvolved DC shift image includes full bandwidth information. Therefore, in the next iteration higher harmonics information is estimated from the deconvolved DC shift image and used for the next reconstruction. In each step, reconstructed image is compared with the ideal x-space MPI image and iterative reconstruction is stopped when recontructed image converges to the ideal MPI image.

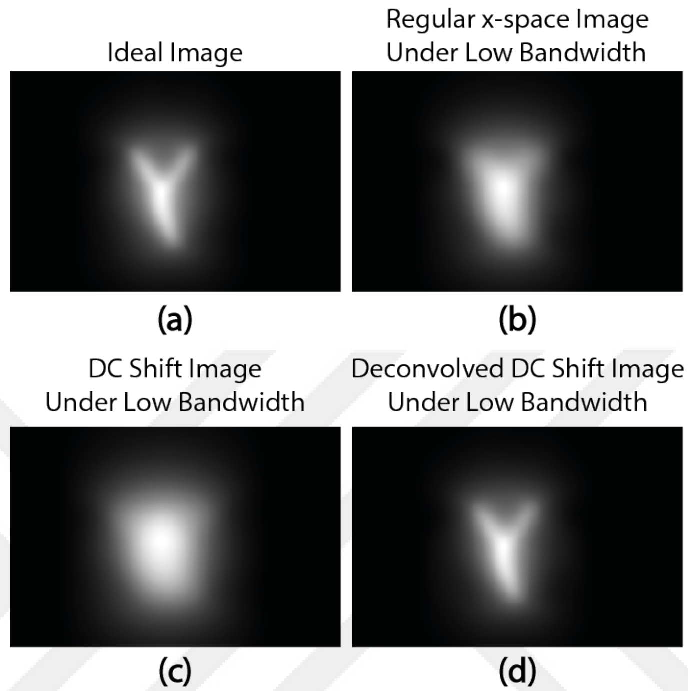

Figure 3.5: Regular x-space and DC shift theory based reconstructions under 2^{nd} and 3^{rd} harmonics acquisition. The a) ideal image that includes all harmonics is less blurred compared to the b) low bandwidth reconstructed image. The c) DC shift image is blurred compared to the regular x-space image under low bandwidth; however, the convolution kernel can be calculated and deconvolution of the DC shift image with the known convolution kernel gives d) deconvolved DC shift image that is very similar to the ideal MPI image.

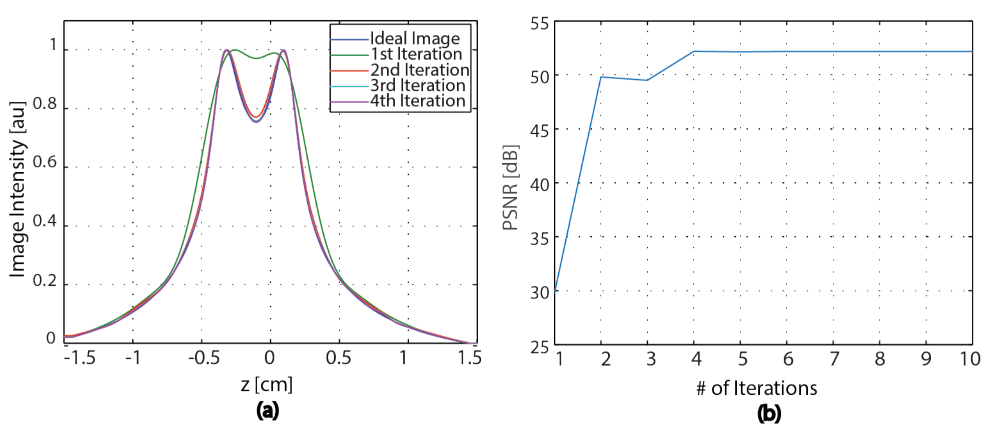

Figure 3.6: PSNR analysis results for ten iterations. The convergence is achieved at the 4^{th} iteration. Therefore, the output of the reconstructed image at the 4^{th} iteration can be used as the resulting x-space MPI image.

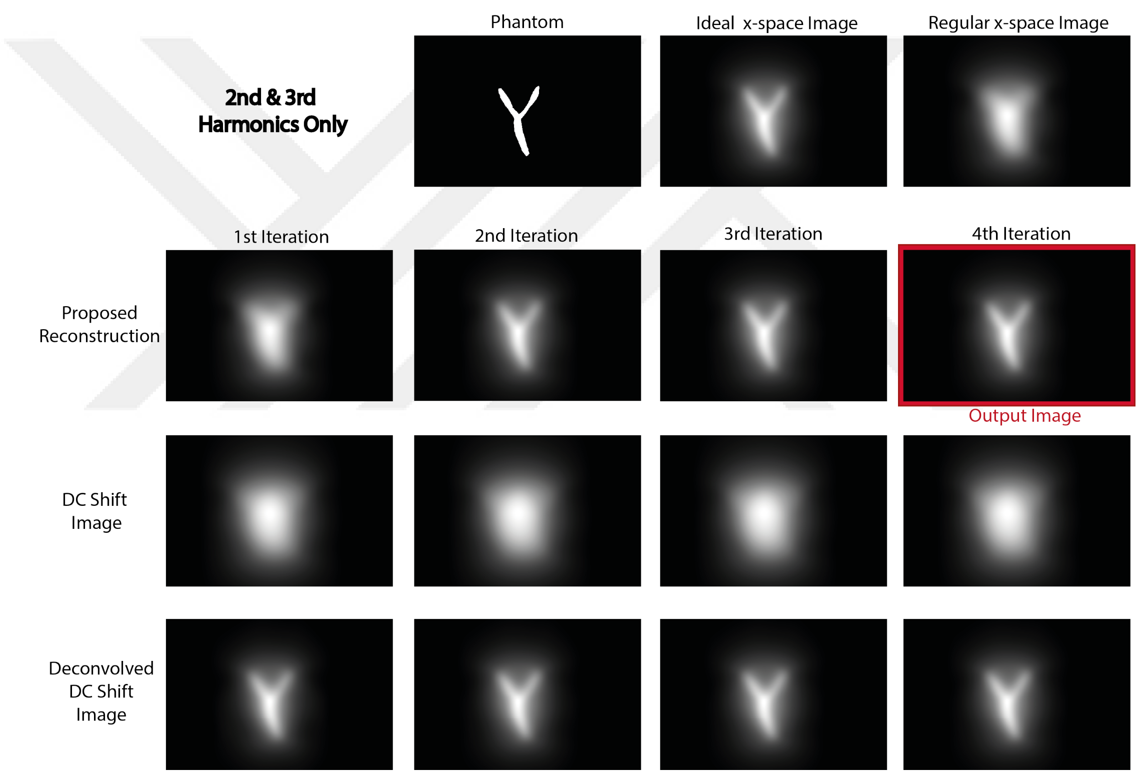

Figure 3.7: Under low-bandwidth acquisition (i.e., 2^{nd} and 3^{rd} harmonics only), regular reconstruction results in blurred images. With the help of deconvolved DC shift image, the lost higher harmonics information can be calculated and used to obtain more reliable images. At the 4^{th} iteration, resulting image gives good match to the ideal x-space image.

Chapter 4

Methods

4.1 Trajectories

In MPI, the human safety thresholds limit the amplitudes of the applied drive fields that in turn cause the limited size of pFOVs. Therefore, an additional magnetic field called “focus field” is used to enlarge the imaging region [2, 14, 17]. In this thesis, two different trajectories were used for the simulations. In the following sections, the details of the trajectories will be explained in detail.

4.1.1 Step-wise Trajectory

In the step-wise trajectory, a sinusoidal drive field determines the size of the pFOV and allows to image pFOV with a back and forth scan. The drive field frequency is around kHz range and generally each pFOV is scanned with more than one cycle. Therefore, one pFOV image can be obtained by averaging of all cycles that allows to obtain more reliable pFOV image especially under noise effect. In order to enlarge the imaging region, relatively small piecewise constant focus field is applied. This focus field shifts the center of the pFOV such that at there is an overlapping section between the neighboring pFOVs. Overlap percentage is important to determine the continuity in image domain with a high accuracy. The overlap percent is given as one of the scan parameters and then the number of pFOVs for the given image size can be calculated.

4.1.2 Linear Trajectory

In the linear trajectory, a linearly increasing focus field is applied simultaneously with the drive field [28, 29, 30]. Therefore, depending on the slew rate of the focus field, slow or fast scanning can be obtained. In the linear trajectory, slew rate is one of the scan parameters and depending on the slew rate, the overlap percentage and the number of pFOVs can be calculated. In real-life applications, the linear trajectory would be preferred over the step-wise trajectory due to its increased speed in covering a specified FOV size. In the simulations, the performance of the proposed method was considered for both the step-wise and linear trajectories, as shown in Figure 4.1.

4.2 Simulation Parameters

In the simulations, the gradient strength of the selection field was 6 T/m and 3 T/m in x and z directions, respectively. The drive field amplitude was 10 mT and the frequency was 25 kHz. 25 nm magnetic nanoparticle diameter was used. To avoid low-SNR regions of each pFOV, a cut percent of 20% was utilized, which removes the regions of pFOV where the FFP speed is below 20% of its maximum value. In the step-wise trajectory, the overlap was 95% and in the linear trajectory, the slew rate was 20 T/s. For the simulations that include relaxation, images were reconstructed using the non-adiabatic x-space imaging equation described in [23] and the relaxation time constant was 1 μs. The signal is periodic in step-wise trajectory so in frequency domain, there are distinct peaks at each harmonic position. Therefore, filtering in this trajectory was simple for low bandwidth acquisition. In the linear trajectory, however, the signal is not periodic and due to this reason it is possible to see non-harmonic signals in

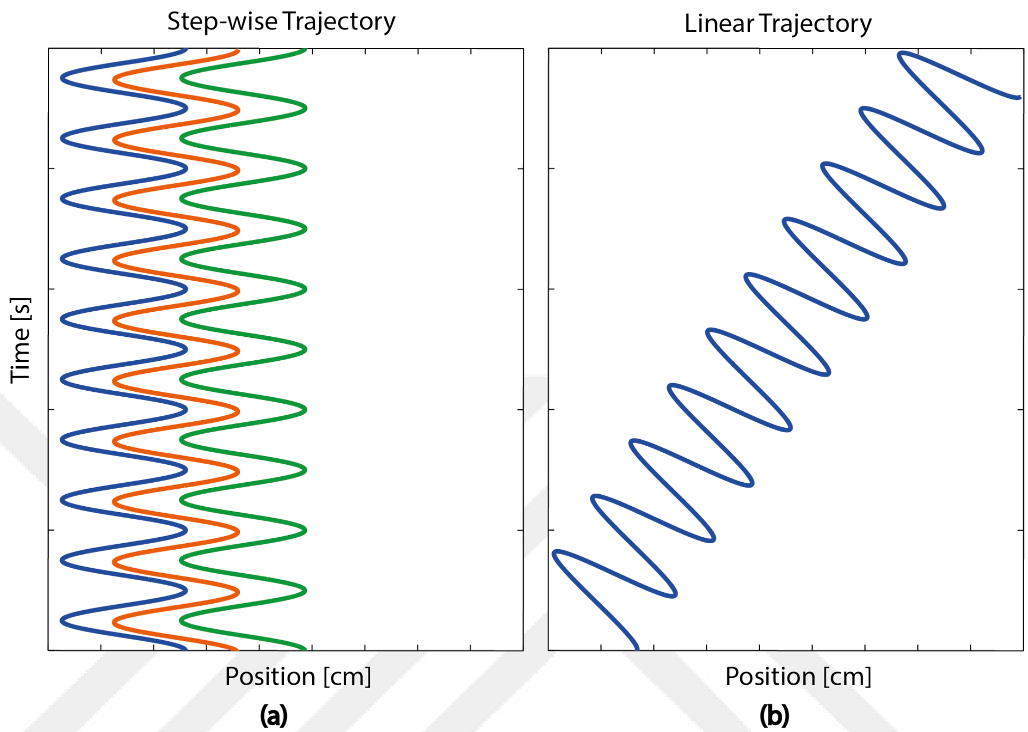

Figure 4.1: Trajectories used in simulations. a) Step-wise trajectory, where a piecewise constant focus field is used to move pFOV and b) linear trajectory, where linearly increasing focus field is used. Linear trajectory is faster than the step-wise trajectory.

the frequency domain, which results in visible artifacts in image domain for the proposed reconstruction. To solve this problem, the non-harmonic signals that are not in the range of $\pm 20\%$ around the harmonic frequencies were filtered out. A Lucy-Richardson deconvolution with edge tapering was applied with iteration number 50 to reconstruct the deconvolved DC shift image at each step of the iterative reconstruction.

4.3 Noise Addition

The simulations were done for different signal SNR values starting from 30 dB to 5 dB. The SNR value is given as one of the simulation parameters and depending on the value of the SNR, the standard deviation of the noise is calculated. To determine the standard deviation of the noise, the maximum value of the signal is divided to the desired signal SNR value. Next, white Gaussian noise is generated using the calculated standard deviation and then added to the ideal magnetic nanoparticle signal.

4.4 DC Shift Imaging

When all DC shift values are calculated, it is observed that some of them are negative. In theory, the DC shift image is the convolution of the ideal MPI image with a kernel, which are both positive valued. Hence, ideally, the DC shift values should not be negative. Here, the DC shift values are enforced to be nonnegative by shifting up all DC values such that the minimum DC shift value is zero. Then, it is observed that although one end of the FOV has zero DC shift value, the other end is greater than zero. In the deconvolution steps, all ends should go to zero. Otherwise, ringing artifacts are observed in the resulting image. In order to prevent ringing artifacts problem in the deconvolved DC shift image, an extrapolation is done by extending the size of the DC shift image until it hits zero at both ends. In practice, zeroes are assigned to both ends of an extended DC shift image and an interpolation is applied to calculate the missing points. The deconvolution is done using the extended DC shift image; therefore, the resulting deconvolved DC shift image is also extended. The original FOV part of the deconvolved DC shift image is selected as the center part.

4.5 Averaging

In all simulations, reconstructed images are obtained using the averaging of images obtained during the positive and negative scans of the pFOVs. Although positive and negative images are the same for the ideal case (i.e., no noise and no relaxation case) with step-wise trajectory due to periodicity, they are different when other cases are considered.

4.6 Scanner Parameters

An in-house MPI scanner was developed in Bilkent University, National Magnetic Resonance Research Center (UMRAM). The scanner operates at 9.7 kHz and the gradients of the selection field are [Gx Gy Gz] =[-4.8 2.4 2.4] T/m. Applied drive field amplitude can be up to 40 mT. The scanner utilizes step-wise trajectory and the focus field concept is implemented mechanically using robot arms. The FOV size is 1x1x10 cm^3 in x, y and z directions, respectively. The size of the FOV_z is limited only by the length of the robot arm. The sampling frequency is 2 MHz. In addition to that, the self-resonance of the receive coil is around 280 kHz, which limit the range of usable harmonics.

4.7 Experimental Setup Parameters

The performance of the proposed reconstruction was evaluated on the experimental data. For this, a phantom with 2 tubes were filled with Perimag magnetic nanoparticles. The diameter of each tube was 2 mm. The concentration of the Perimag nanoparticles is 17 mg Fe/mL and the dilution ratio was 1:10. The concentrations of the two tubes were almost the same. These samples were imaged using 15 mT drive field at 9.7 kHz. The gradients of the selection field were [Gx Gy Gz] =[-4.8 2.4 2.4] T/m. The overlap percentage was selected as 95% and the pFOV size is 1.25 cm with $FOV_z = 6.5$ cm and $FOV_x = 0.8$ cm. The number of lines along the z-direction was 9 (i.e., FOV_x is sampled at 9 points).

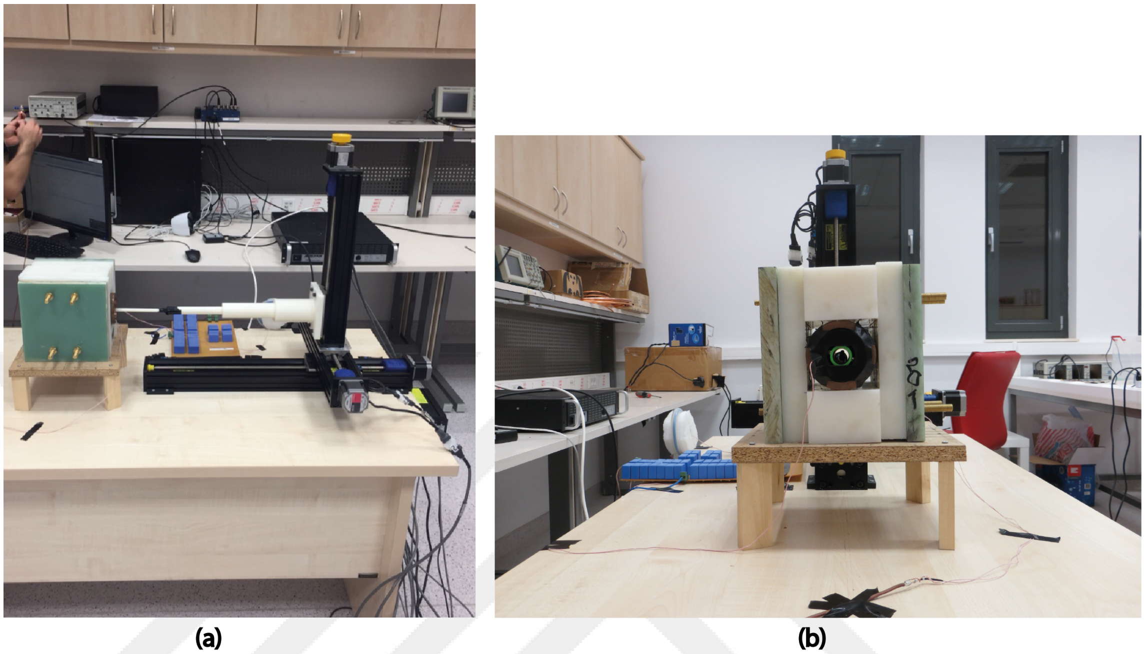

Figure 4.2: In house MPI scanner built in National Magnetic Resonance Research Center (UMRAM), Bilkent University. a) and b) shows the side views of the scanner.

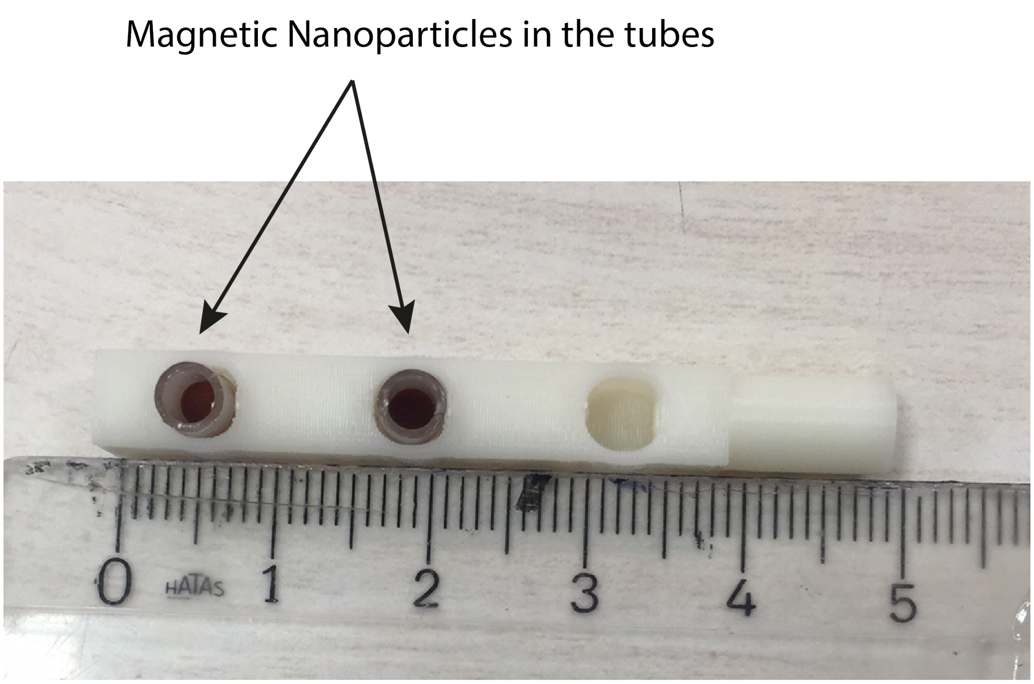

Figure 4.3: The phantom used in 2D imaging experiments. Perimag nanoparticles were used. The concentrations of the both tubes were almost the same.

Chapter 5

Results

The proposed method was evaluated with extensive simulations and imaging experiments. For the simulations, two different trajectory types were used and the performance of the proposed method was evaluated using PSNR metric for both trajectories.

5.1 Simulation Results

5.1.1 Step-wise Trajectory

The proposed method was tested firstly on the step-wise trajectory. Under both noise-only and noise & relaxation cases, both the regular x-space MPI and proposed reconstruction images were reconstructed under different signal SNR levels. The highest and the lowest SNR values were selected as 30 dB and 5 dB, respectively. The results were compared with the noise free case results, as well. Using the PSNR metric, the success of the proposed method was evaluated.

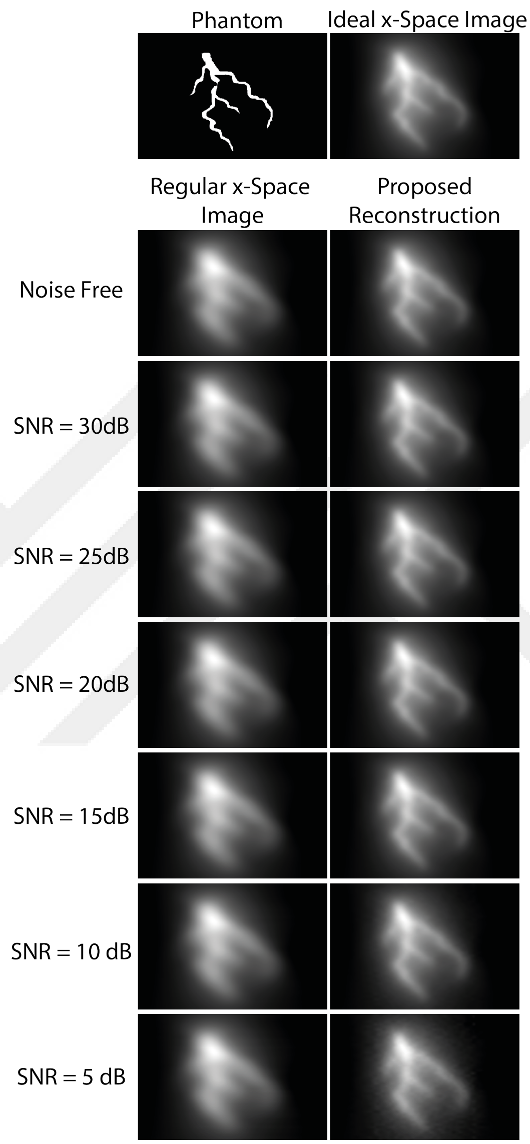

Figure 5.1: Regular and proposed reconstruction results under different noise levels. Step-wise trajectory was used. 10 mT, 25 kHz drive field with 95% overlap was used.

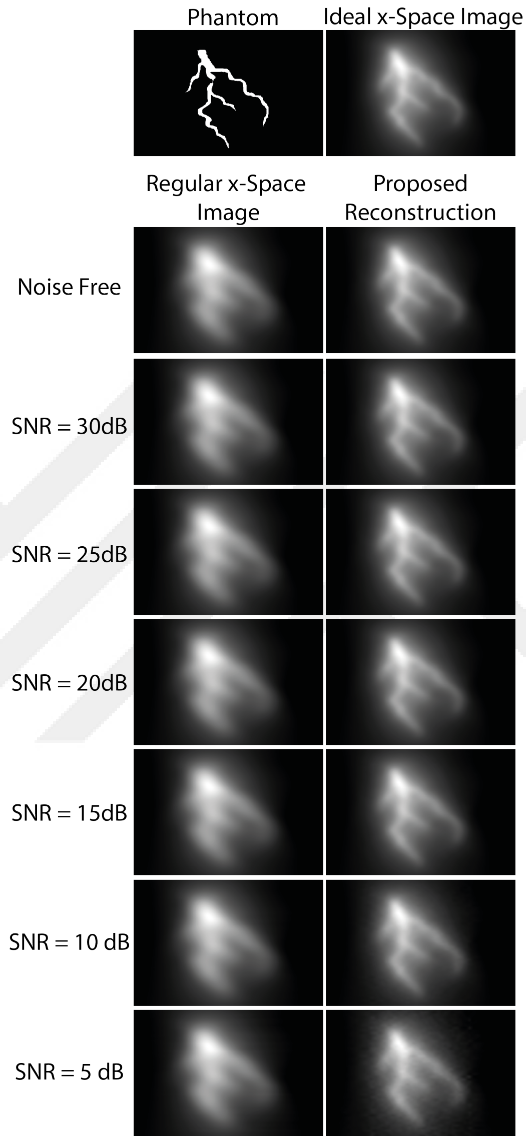

Figure 5.2: Regular and proposed reconstruction results under noise and relaxation effects. Step-wise trajectory was used. 10 mT, 25 kHz drive field with 95% overlap was used.

The first simulations were done for the noise-only case. As it can be seen from Figure 5.1, due to the low-bandwidth acquisition, the regular x-space reconstruction resulted in very blurred images. The improvement in the proposed method can be seen from the PSNR analysis as in Table 5.1. When noise free case is considered, the PSNR for the regular reconstruction is 32 dB. Iterative reconstruction using DC shift theory results in 48 dB peak-SNR for the proposed reconstruction. Until 5 dB signal SNR, the improvent in the proposed reconstruction is around 16 dB, which is a significant improvement. At very low SNR values, there is still 13 dB improvement in the proposed reconstruction.

SNR [dB]	PSNR for Regular Reconstruction [dB]	PSNR for Proposed Reconstruction [dB]
No Noise	32	48
30	32	48
25	32	48
20	32	48
15	32	49
10	32	46
5	32	45

Table 5.1: PSNR analysis for noise only case for step-wise trajectory

The proposed method is also evaluated under both noise and relaxation effects as shown in Figure 5.2. The improvement in the proposed method can be seen from the PSNR analysis table for the step-wise trajectory. There is at least 9 dB improvement in the proposed reconstruction at 5 dB SNR level. As the SNR increases, the improvement is nearly 13 dB.

SNR [dB]	PSNR for Regular Reconstruction [dB]	PSNR for Proposed Reconstruction [dB]
No Noise	32	45
30	32	45
25	32	45
20	32	45
15	32	45
10	32	44
5	31	40

Table 5.2: PSNR analysis for noise and relaxation case for step-wise trajectory

5.1.2 Linear Trajectory

Similar analysis for both noise-only and noise & relaxation cases were done for the linear trajectory, as well. The resulting images for both regular and proposed reconstruction under the noise effect are shown as in Figure 5.3. For linear trajectory, although regular reconstruction results in nearly 32 dB PSNR, proposed method shows an important improvement on the reconstructed images around 49-50 dB for high SNR levels and for very low SNR levels, it is possible to obtain a significant amount of improvement around 9-11 dB. If both noise and relaxation effects are considered, the resulting images and PSNR analysis become as in Figure 5.4 and Table 5.4.

SNR [dB]	PSNR for Regular Reconstruction [dB]	PSNR for Proposed Reconstruction [dB]
No Noise	32	50
30	32	50
25	32	50
20	32	49
15	32	49
10	31	42
5	31	40

Table 5.3: PSNR analysis for noise only case for linear trajectory

SNR [dB]	PSNR for Regular Reconstruction [dB]	PSNR for Proposed Reconstruction [dB]
No Noise	32	49
30	32	49
25	32	49
20	32	49
15	32	47
10	31	44
5	29	35

Table 5.4: PSNR analysis for noise and relaxation case for linear trajectory

As it is seen from Figure 5.4 and Table 5.4 , proposed reconstruction is significantly better than the regular x-space reconstruction. When the PSNR results are compared, it can be said that there is at least 6 dB improvement on the reconstructed proposed image.

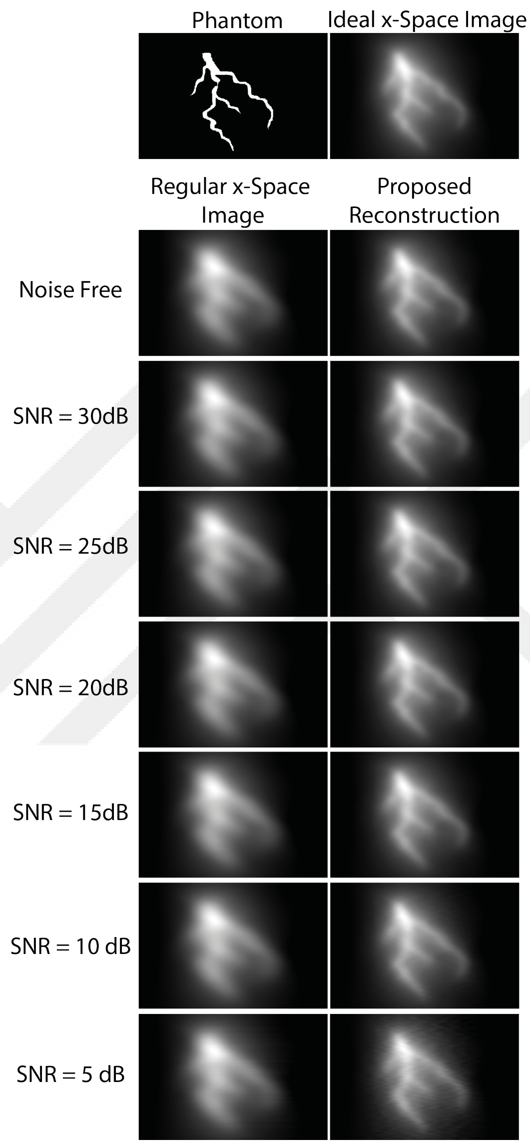

Figure 5.3: Regular and proposed reconstruction results under different noise levels. Linear trajectory was used. 10 mT, 25 kHz drive field with 20 T/s slew rate was used.

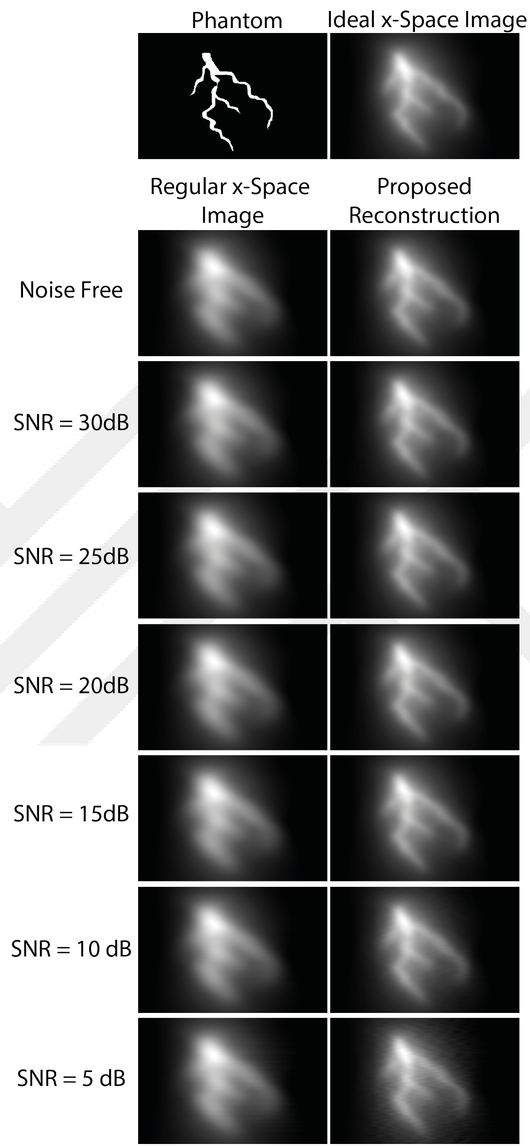

Figure 5.4: Regular and proposed reconstruction results under different noise and relaxation effects. Linear trajectory was used. 10 mT, 25 kHz drive field with 20 T/s slew rate was used.

5.2 Experimental Results

The performance of the proposed reconstruction method was also evaluated on experimental data. As it is seen from the Figure 5.5, two tubes were filled with similar amounts of Perimag magnetic nanoparticles. After imaging experiments, using regular x-space reconstruction method, different signal bandwidth levels were evaluated. Similar to the simulation results, as the bandwidth becomes narrower, due to the loss of higher harmonics, reconstructed regular x-space image becomes blurred. For 2^{nd} and 3^{rd} harmonics only case, the iterative reconstruction was applied and the proposed reconstruction result (i.e., the result of 4^{th} iteration) gave better result than the [2 : 10] harmonics bandwidth case. Note that while the phantoms were circular, the reconstructed MPI images were not fully circular. This can be due to the non-perfect circular shape of the manually-made phantom.

These seen in the Figure 5.5, the results of the proposed reconstruction displayed better resolution when compared to regular x-space reconstructed images. These results experimentally verify the improvement that can be achieved using the proposed iterative reconstruction technique.

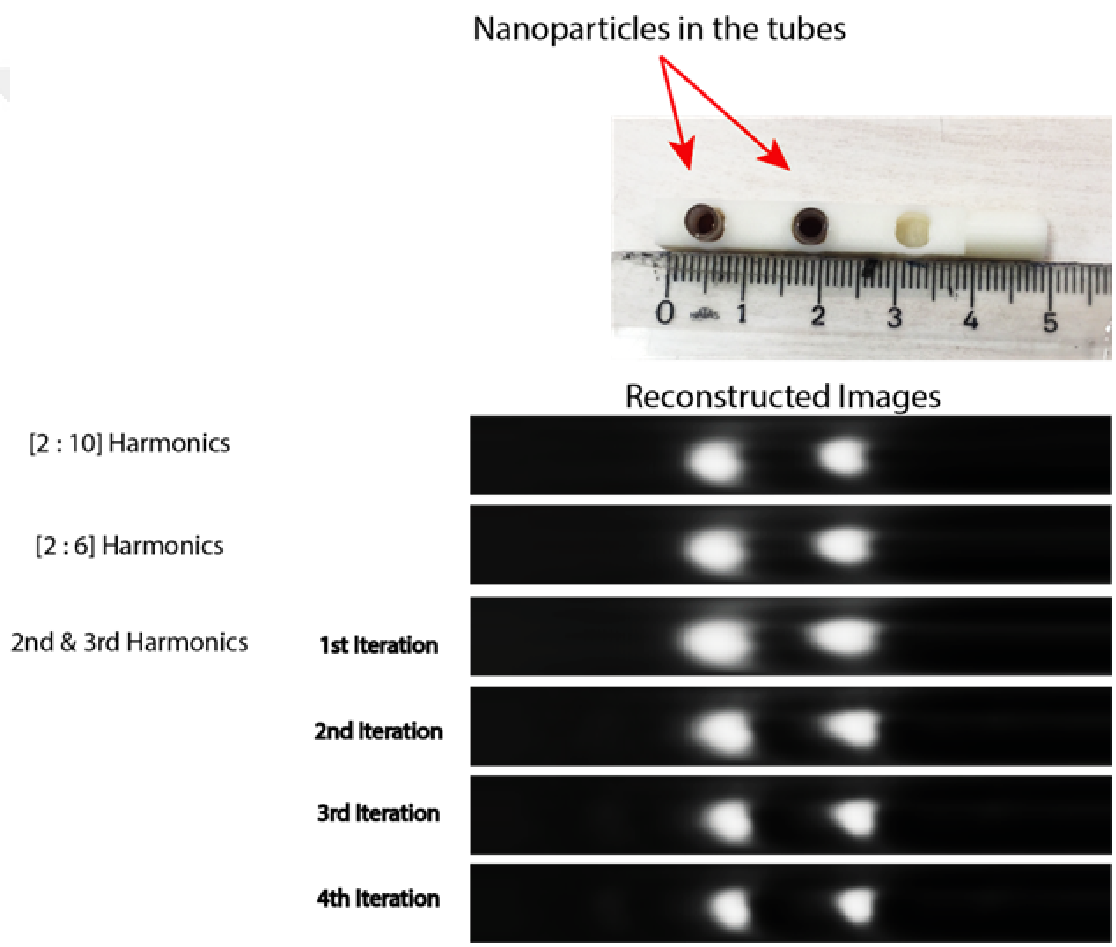

Figure 5.5: Experimental validation of the proposed iterative reconstruction. Step-wise trajectory was used. 15 mT, 9.7 kHz drive field with 95% overlap.

Chapter 6

Discussion and Conclusion

Image reconstruction is one of the most important topics in x-space MPI. Until now, regular x-space reconstruction technique was used to obtain the resulting x-space MPI image. As shown in Chapter 3, using DC shift theory for full-bandwidth acquisitions, it is possible to reconstruct an image that closely matches the regular x-space MPI image. This thesis proposed an iterative reconstruction technique based on DC shift theory for low-bandwidth signal acquisitions. While regular x-space reconstruction results in blurred images under low-bandwidth signal acquisitions, the proposed iterative reconstuction recovers the un-acquired higher harmonics to yield images with increased resolution.

To increase the effectiveness of the proposed reconstruction, it is important to sample the DC shift values finely with the purpose of obtaining more reliable DC shift images. The distance between the DC shift values (i.e., the distance between pFOV centers) should be comparable to the FWHM of the imaging PSF, which in turn requires high overlap percentages and/or small drive field amplitudes. While these constraints may sound limiting, in fact the human safety limits in MPI naturally force the data acquisition to these conditions. Hence, the proposed technique is practical when human safety limits are considered.

Proposed method was tested using two different trajectories. In the linear trajectory, due to the non-periodicity, it is possible to observe non-harmonic signals that eventually result in artifacts especially in the deconvolved DC shift image. Since the DC shift image is used in the proposed reconstruction process, similar artifacts may also occur in the final reconstructed image. Here, to eliminate this artifact, a filter that eliminates frequencies that are not within $(^{+}_{-})$ $0.2f_0$ of the higher harmonics was used.

Due to the finite extent of the FOV covered during imaging, the deconvolution process may yield ringing artifacts in the final image. To decrease the effect of this artifact, the DC shift image should be extended on both sides, such that the pixel intensities fade to zero gradually. Here, this step was performed via a spline interpolation in the extended regions.

The proposed method can be successfully applied to low-bandwidth MPI data for x-space MPI trajectories that cover the region of interest in a line-by-line fashion. Here, the proposed method was demonstrated for the case of acquiring only the 2^{nd} and the 3^{rd} harmonics. Further analysis revealed that these two harmonics are essential for this technique to work reliably. Obtaining only the 2^{nd} or only the 3^{rd} harmonics results in less reliable images, with visible artifacts on the reconstructed images.

The proposed iterative low-bandwith reconstruction technique is robust against low SNR, implying that it is well suited for imaging even small doses of administered SPIO. Future work includes experimentally demonstrating the proposed method for linear trajectories. Further work may also involve comparing image quality across different concentration levels of nanoparticles.

Bibliography

[1] B. Gleich and J. Weizenecker, "Tomographic imaging using the nonlinear response of magnetic particles," *Nature*, vol. 435, pp. 1214–1217, 2005.

[2] J. Weizenecker, B. Gleich, J. Rahmer, H. Dahnke, and J. Borgert, "Three-dimensional real-time in vivo magnetic particle imaging," *Physics in Medicine and Biology*, vol. 54, no. 5, pp. L1–L10, 2009.

[3] P. W. Goodwill, E. U. Saritas, L. R. Croft, T. N. Kim, K. M. Krishnan, D. V. Schaffer, and S. M. Conolly, "X-space mpi: Magnetic nanoparticles for safe medical imaging," *Advanced Materials*, vol. 24, no. 28, pp. 3870–3877, 2012.

[4] J. Weizenecker, J. Borgert, and B. Gleich, "A simulation study on the resolution and sensitivity of magnetic particle imaging," *Physics in Medicine and Biology*, vol. 52, no. 21, p. 6363, 2007.

[5] E. U. Saritas, P. W. Goodwill, L. R. Croft, J. J. Konkle, K. Lu, B. Zheng, and S. M. Conolly, "Magnetic particle imaging mpi for nmr and mri researchers," *J. Magn. Reson.*, vol. 229, pp. 116–126, 2013.

[6] L. M. Bauer, S. F. Situ, M. A. Griswold, and A. C. Samia, "Magnetic particle imaging tracers: State-of-the-art and future directions," *J Phys Chem Lett*, vol. 6, no. 13, pp. 2509–2517, 2015.

[7] B. Zheng, T. Vazin, P. W. Goodwill, A. Conway, A. Verma, E. U. Saritas, D. Schaffer, and S. M. Conolly, "Magnetic particle imaging tracks the long-term fate of in vivo neural cell implants with high image contrast," *Sci Rep*, vol. 5, p. 14055, 2015.

[8] B. Zheng, M. P. von See, E. Yu, B. Gunel, K. Lu, T. Vazin, D. V. Schaffer, P. W. Goodwill, and S. M. Conolly, "Quantitative magnetic particle imaging monitors the transplantation, biodistribution, and clearance of stem cells in vivo," *Theranostics*, vol. 6, no. 3, pp. 291–301, 2016.

[9] K. Them, J. Salamon, P. Szwargulski, S. Sequeira, M. G. Kaul, C. Lange, H. Ittrich, and T. Knopp, "Increasing the sensitivity for stem cell monitoring in system-function based magnetic particle imaging," *Phys Med Biol*, vol. 61, no. 9, pp. 3279–3290, 2016.

[10] J. Haegele, J. Rahmer, B. Gleich, J. Borgert, H. Wojtczyk, N. Panagiotopoulos, T. M. Buzug, J. Barkhausen, and F. M. Vogt, "Magnetic particle imaging: visualization of instruments for cardiovascular intervention," *Radiology*, vol. 265, no. 3, pp. 933–938, 2012.

[11] P. W. Goodwill and S. M. Conolly, "The x-space formulation of the magnetic particle imaging process: 1-d signal, resolution, bandwidth, snr, sar, and magnetostimulation," *IEEE Transactions on Medical Imaging*, vol. 29, no. 11, pp. 1851–1859, 2010.

[12] J. Rahmer, J. Weizenecker, B. Gleich, and J. Borgert, "Signal encoding in magnetic particle imaging: properties of the system function," *BMC Med Imaging*, vol. 9, p. 4, 2009.

[13] J. Rahmer, J. Weizenecker, B. Gleich, and J. Borgert, "Analysis of a 3-D system function measured for magnetic particle imaging," *IEEE Trans Med Imaging*, vol. 31, no. 6, pp. 1289–1299, 2012.

[14] E. U. Saritas, P. W. Goodwill, G. Z. Zhang, and S. M. Conolly, "Magnetostimulation limits in magnetic particle imaging," *IEEE Transactions on Medical Imaging*, vol. 32, no. 9, pp. 1600–1610, 2013.

[15] E. U. Saritas, P. W. Goodwill, and S. M. Conolly, "Effects of pulse duration on magnetostimulation thresholds," *Med Phys*, vol. 42, no. 6, pp. 3005–3012, 2015.

[16] O. B. Demirel and E. U. Saritas, "Effects of duty cycle on magnetostimulation thresholds in mpi," *International Journal on Magnetic Particle Imaging*, vol. 3, no. 1, 2017.

[17] J. Rahmer, B. Gleich, J. Schmidt, I. Schmale, C. Bontus, J. Kanzenbach, J. Borgert, O. Woywode, and J. Weizenecker, "Increased volume coverage in 3d magnetic particle imaging," in *Proceedings of the 4th International Symposium on Applied Sciences in Biomedical and Communication Technologies*, pp. 1–5, 2011.

[18] K. Lu, P. W. Goodwill, E. U. Saritas, B. Zheng, and S. M. Conolly, "Linearity and shift invariance for quantitative magnetic particle imaging," *IEEE Transactions on Medical Imaging*, vol. 32, no. 9, pp. 1565–1575, 2013.

[19] S. Ota, R. Takeda, T. Yamada, I. Kato, S. Nohara, and Y. Takemura, "Effect of particle size and structure on harmonic intensity of blood-pooling multicore magnetic nanoparticles for magnetic particle imaging," *International Journal on Magnetic Particle Imaging*, vol. 3, no. 1, 2017.

[20] T. Yoshida, T. Sasayama, and K. Enpuku, "Effect of core size distribution of immobilized magnetic nanoparticles on harmonic magnetization," *International Journal on Magnetic Particle Imaging*, vol. 3, no. 1, 2017.

[21] T. Knopp and T. M. Buzug, *How Magnetic Particle Imaging Works*, pp. 11–70. Springer Berlin Heidelberg, 2012.

[22] R. Dhavalikar, D. Hensley, L. Maldonado-Camargo, L. R. Croft, S. Ceron, P. W. Goodwill, S. M. Conolly, and C. Rinaldi, "Finite magnetic relaxation in x-space magnetic particle imaging: Comparison of measurements and ferrohydrodynamic models," *J Phys D Appl Phys*, vol. 49, no. 30, 2016.

[23] L. R. Croft, P. W. Goodwill, and S. M. Conolly, "Relaxation in x-space magnetic particle imaging," *IEEE Trans Med Imaging*, vol. 31, no. 12, pp. 2335–2342, 2012.

[24] H. Arami, R. M. Ferguson, A. P. Khandhar, and K. M. Krishnan, "Size-dependent ferrohydrodynamic relaxometry of magnetic particle imaging tracers in different environments," *Med Phys*, vol. 40, no. 7, p. 071904, 2013.

[25] D. Sarica and E. U. Saritas, "Effects of field dependent relaxation time on x-space mpi images," in *2015 5th International Workshop on Magnetic Particle Imaging (IWMPI)*, pp. 1–1, 2015.

[26] P. W. Goodwill and S. M. Conolly, "Multidimensional x-space magnetic particle imaging," *IEEE Trans Med Imaging*, vol. 30, no. 9, pp. 1581–1590, 2011.

[27] D. Sarica, O. B. Demirel, Y. Muslu, and E. U. Saritas, "Dc shift imaging for x-space mpi reconstruction," *In International Workshop on Magnetic Particle Imaging*, 2016.

[28] P. W. Goodwill, J. J. Konkle, B. Zheng, E. U. Saritas, and S. M. Conolly, "Projection x-space magnetic particle imaging," *IEEE Trans Med Imaging*, vol. 31, no. 5, pp. 1076–1085, 2012.

[29] J. J. Konkle, P. W. Goodwill, E. U. Saritas, B. Zheng, K. Lu, and S. M. Conolly, "Twenty-fold acceleration of 3d projection reconstruction mpi," *Biomed Tech (Berl)*, vol. 58, no. 6, pp. 565–576, 2013.

[30] O. B. Demirel, D. Sarica, and E. U. Saritas, "Rapid scanning in x-space mpi: Impacts on image quality," *In International Workshop on Magnetic Particle Imaging*, 2016.